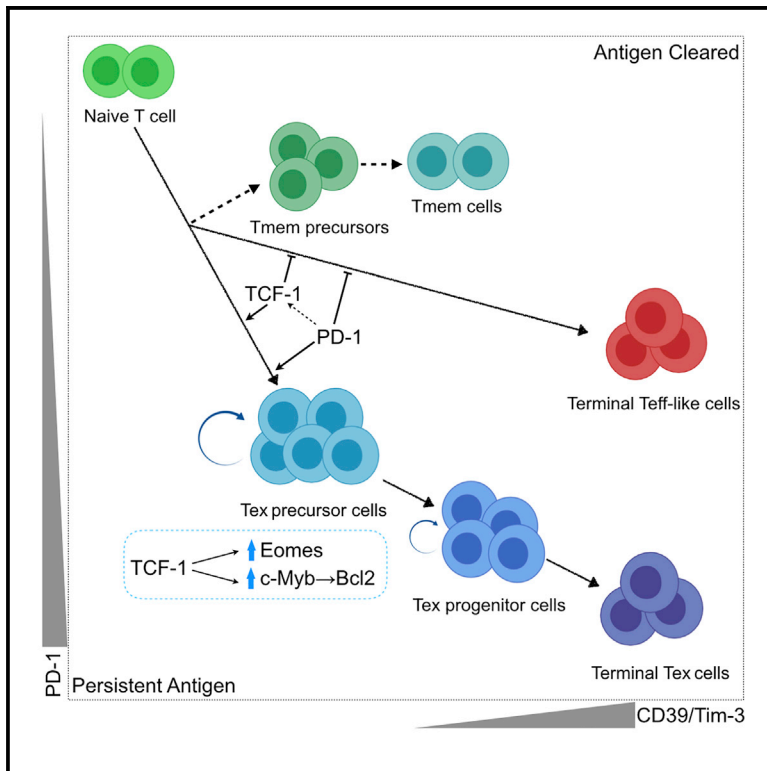


TCF-1-Centered Transcriptional Network Drives an Effector versus Exhausted CD8 T Cell-Fate Decision

Graphical Abstract



Authors

Zeyu Chen, Zhicheng Ji, Shin Foong Ngiow, ..., Golnaz Vahedi, Hongkai Ji, E. John Wherry

Correspondence

wherry@pennmedicine.upenn.edu

In Brief

The initiation of the T cell exhaustion program remains poorly understood. In this study, Chen et al. define an effector (Teff) versus exhausted (Tex) CD8 T cell binary-fate decision during chronic infection and find that TCF-1 supports the Tex precursor development by antagonizing Teff-like cell differentiation through multiple transcription factors.

Highlights

- scRNA-seq defines an effector versus exhausted Tex cell-fate decision
- TCF-1 plays a central role in initially establishing Tex precursor cells
- PD-1 supports the TCF-1⁺ Tex precursor cells at early phase of chronic infection
- Eomes and c-Myb play key roles in Tex cell persistence downstream of TCF-1



TCF-1-Centered Transcriptional Network Drives an Effector versus Exhausted CD8 T Cell-Fate Decision

Zeyu Chen,^{1,2,13} Zhicheng Ji,^{3,13} Shin Foong Ngiow,^{1,2} Sasikanth Manne,^{1,2} Zhangying Cai,^{1,2} Alexander C. Huang,^{1,2,4} John Johnson,² Ryan P. Staupe,^{1,2} Bertram Bengsch,^{1,2,11} Caiyue Xu,^{5,6} Sixiang Yu,⁷ Makoto Kurachi,^{1,2,12} Ramin S. Herati,^{1,2,4} Laura A. Vella,^{1,2,8} Amy E. Baxter,^{1,2} Jennifer E. Wu,^{1,2} Omar Khan,^{1,2} Jean-Christophe Beltra,^{1,2} Josephine R. Giles,^{1,2} Erietta Stelekati,^{1,2} Laura M. McLane,^{1,2} Chi Wai Lau,^{1,2} Xiaolu Yang,⁷ Shelley L. Berger,^{5,6} Golnaz Vahedi,^{2,6,9} Hongkai Ji,³ and E. John Wherry^{1,2,10,14,*}

¹Department of Systems Pharmacology and Translational Therapeutics, Perelman School of Medicine, University of Pennsylvania, Philadelphia, PA 19104, USA

²Institute for Immunology, Perelman School of Medicine, University of Pennsylvania, Philadelphia, PA 19104, USA

³Department of Biostatistics, Johns Hopkins Bloomberg School of Public Health, Baltimore, MD 21205, USA

⁴Department of Medicine, Perelman School of Medicine, University of Pennsylvania, Philadelphia, PA 19104, USA

⁵Department of Cell and Developmental Biology, Perelman School of Medicine, University of Pennsylvania, Philadelphia, PA 19104, USA

⁶Epigenetics Institute, Perelman School of Medicine, University of Pennsylvania, Philadelphia, PA 19104, USA

⁷Department of Cancer Biology, Perelman School of Medicine, University of Pennsylvania, Philadelphia, PA 19104, USA

⁸Department of Pediatrics, Children's Hospital of Philadelphia, Philadelphia, PA 19104, USA

⁹Department of Genetics, Perelman School of Medicine, University of Pennsylvania, Philadelphia, PA 19104, USA

¹⁰Parker Institute for Cancer Immunotherapy at University of Pennsylvania, Philadelphia, PA 19104, USA

¹¹Present address: Department of Medicine II, Gastroenterology, Hepatology, Endocrinology, and Infectious Diseases, Faculty of Medicine, University Medical Center Freiburg, 79106 Freiburg, Germany

¹²Present address: Department of Biochemistry I, Graduate School of Medical Sciences, Kanazawa University, Kanazawa, Ishikawa Prefecture 920-1192, Japan

¹³These authors contributed equally

¹⁴Lead Contact

*Correspondence: wherry@penmedicine.upenn.edu

<https://doi.org/10.1016/j.immuni.2019.09.013>

SUMMARY

TCF-1 is a key transcription factor in progenitor exhausted CD8 T cells (Tex). Moreover, this Tex cell subset mediates responses to PD-1 checkpoint pathway blockade. However, the role of the transcription factor TCF-1 in early fate decisions and initial generation of Tex cells is unclear. Single-cell RNA sequencing (scRNA-seq) and lineage tracing identified a TCF-1⁺Ly108⁺PD-1⁺ CD8 T cell population that seeds development of mature Tex cells early during chronic infection. TCF-1 mediated the bifurcation between divergent fates, repressing development of terminal KLRG1^{Hi} effectors while fostering KLRG1^{Lo} Tex precursor cells, and PD-1 stabilized this TCF-1⁺ Tex precursor cell pool. TCF-1 mediated a T-bet-to-Eomes transcription factor transition in Tex precursors by promoting Eomes expression and drove c-Myb expression that controlled Bcl-2 and survival. These data define a role for TCF-1 in early-fate-bifurcation-driving Tex precursor cells and also identify PD-1 as a protector of this early TCF-1 subset.

INTRODUCTION

During acute infections or vaccinations, naive CD8 T cells become activated and differentiate into a pool of effector

T cells containing KLRG1^{Hi} terminal effector (Teff) cells and KLRG1^{Lo}CD127^{Hi} memory precursor (Tmp) cells (Kaech and Cui, 2012). The KLRG1^{Hi} Teff cell population is often 5–20 times more numerous than the Tmp cell subset and has robust effector functions. However, the KLRG1^{Hi} population is terminal, largely disappearing over the ensuing weeks, whereas the Tmp cell population matures into long-term memory CD8 T cells (Kaech et al., 2003). During chronic infections or in tumors, the KLRG1^{Hi} population of Teff (or the related effector memory RA CD8 T cells [Temra] or CD57⁺ populations in humans) cells is less prominent (Angelosanto et al., 2012; Joshi et al., 2007; Omilusik et al., 2018), and exhausted CD8 T cells (Tex) that are often found in these settings are KLRG1^{Lo} (Doering et al., 2012; Wherry et al., 2007). Moreover, lineage-tracing studies demonstrated that the KLRG1^{Hi} Teff cell subset survives poorly during chronic infection and cannot give rise to Tex cells (Angelosanto et al., 2012). In contrast, a CD127^{Hi}KLRG1^{Lo} population in the effector phase has the potential to give rise to either functional memory CD8 T cells or Tex cells during acutely resolved or chronic viral infection (Angelosanto et al., 2012). Nevertheless, the developmental paths that seed the formation of Tex cells in chronic infections and cancer remain poorly understood. Dissecting these developmental relationships and the underlying transcriptional circuits could provide opportunities to avoid or reverse T cell exhaustion therapeutically.

Transcriptional control mechanisms have begun to be dissected for developing Teff and Tmp cells following acute infections. The KLRG1^{Hi} Teff cell subset uses the transcription factors (TFs) that foster effector molecule expression



(Kaech and Cui, 2012): T-bet (Joshi et al., 2007), Blimp-1 (Kalles et al., 2009; Rutishauser et al., 2009), Id2 (Yang et al., 2011), and Zeb2 (Dominguez et al., 2015; Guan et al., 2018). Conversely, the KLRG1⁺CD127⁺ Tmp cell fate employs a distinct transcriptional control circuit that includes Eomes (Intlekofer et al., 2005), Bcl-6 (Ichii et al., 2002), Id3 (Yang et al., 2011), TCF-1 (Jeannet et al., 2010), and c-Myb (Chen et al., 2017). This Tmp cell population eventually gives rise to memory CD8 T cells (Tmem) that have the ability to self-renew, persist long term, and provide protection upon subsequent infection (Zhou et al., 2010).

In contrast to acute infections, the early fate commitment steps and regulation of population heterogeneity in initial establishment of CD8 T cell exhaustion remain poorly understood. During chronic infection or cancer, unlike Tmem cells, the Tex cells that develop have decreased function and high expression of inhibitory receptors, such as PD-1, LAG-3, and TIGIT, but relatively low KLRG1 (Wherry et al., 2007). It is now clear that Tex cells are a distinct “lineage” of mature CD8 T cells that differ from Teff and Tmem cells by ~6,000 open chromatin regions (Mognol et al., 2017; Pauken et al., 2016; Philip et al., 2017; Sen et al., 2016). This epigenetic divergence begins early but becomes progressively more widespread and permanent (Pauken et al., 2016; Philip et al., 2017; Sen et al., 2016; Wherry et al., 2007). However, the early transcriptional events that regulate formation of the Tex cell fate compared to Teff or Tmem cell fates remain undefined.

Several transcriptional control mechanisms have been identified in Tex cells. Most notably, T-bet, Eomes, and TCF-1 have been implicated in the biology of Tex cell subsets (He et al., 2016; Im et al., 2016; Paley et al., 2012; Utzschneider et al., 2016; Wu et al., 2016). A Tex cell precursor pool was originally described as a PD-1^{Int} population of Tex cells capable of responding to PD-1 blockade, whereas a more numerous, terminal PD-1^{Hi} subset failed to respond (Blackburn et al., 2008). Subsequent work has identified key roles for T-bet, Eomes, and TCF-1 (He et al., 2016; Im et al., 2016; Paley et al., 2012; Utzschneider et al., 2016; Wu et al., 2016). Nr4a (Chen et al., 2019; Liu et al., 2019), IRF4 (Man et al., 2017), and NFAT (Martinez et al., 2015) have also been implicated in promoting T cell exhaustion, whereas Fosl2 (Stelekati et al., 2018) can partially antagonize exhaustion by promoting memory-like features. Recent work has also shown that the high-mobility group (HMG) protein Tox coordinates the epigenetic imprinting of T cell exhaustion during chronic infections and cancer (Alfei et al., 2019; Khan et al., 2019; Scott et al., 2019; Seo et al., 2019; Yao et al., 2019). Despite these previous studies, the precise sequence of events that leads to the developmental ontogeny of Tex versus Teff and

Tmp cells and subsequent memory remains poorly understood. Furthermore, the mechanism by which TCF-1 shapes Tex cell development remains unclear.

Here, we address these questions about the ontogeny of Tex cells by using a combination of single-cell RNA sequencing (scRNA-seq), computational modeling, lineage tracing, and genetic perturbation to define the early developmental relationships that initiate the Tex cell lineage. scRNA-seq revealed a molecular circuitry in which TCF-1 governed this early Tex cell-fate decision during chronic infection at least in part by repressing an opposing cell fate of terminal Teff cells. TCF-1 antagonized the Teff-cell-driving TFs but positively regulated Eomes and c-Myb. In the latter case, c-Myb then controlled a Bcl-2-dependent survival axis in Tex cells. Moreover, PD-1 expression protected this TCF-1⁺ precursor pool, allowing subsequent formation of mature Tex cells. These analyses revealed that molecular circuitry downstream of TCF-1 functioned at a key fate-decision point between the Tex precursor cells and terminal Teff cell branches of CD8 T cell differentiation. These data fill an important gap between the Tox-initiated epigenetic changes needed for exhaustion and the establishment of fully differentiated Tex cells several weeks later. Moreover, these data suggest that a key mechanism by which TCF-1 promotes the Tex cell developmental program is by antagonizing robust activation involved in the terminal Teff cell differentiation program.

RESULTS

scRNA-Seq Reveals Distinct Subpopulations and Transcriptional Signatures of CD8 T Cells Early during Chronic Viral Infection

To interrogate the early population dynamics during chronic viral infection, we performed scRNA-seq on lymphocytic choriomeningitis virus (LCMV)-D^{GP}₃₃₋₄₁-specific postnatal day 14 (P14) CD8 T cells isolated from naive mice, mice on day 8 (D8) after infection with acutely resolving LCMV Armstrong (Arm), the chronic LCMV clone 13 (Cl13) strain, or mice infected with Cl13 and depleted of CD4 T cells (Cl13ΔCD4) (Figure 1A). We identified 5 major clusters of responding LCMV-specific CD8 T cells (Figure 1B). Cluster 1 contained the majority of cells from D8 Arm, whereas cluster 5 contained almost exclusively naive P14 cells (Figure 1C). D8 Cl13 and Cl13ΔCD4 P14 cells were distributed in clusters 2, 3, and 4 (Figure 1C).

We next examined the top 20 differentially expressed genes across the 5 clusters (Figures 1D and S1A). Cluster 5 expressed naive markers such as *Lef1*, *Ii7r*, *Sell*, *Ccr7*, *Tcf7*, and *Bcl2* (Figures 1D and S1A), consistent with naive CD8 T cells (Tn). Cluster

(B) tSNE clusters of cells from the scRNA-seq.

(C) Cell count of treatment groups across 5 clusters from (B).

(D) Expression of representative genes in tSNE space.

(E) Gene Ontology (GO) enrichment analysis across clusters 1–5. A Bonferroni correction test was performed, and the enrichment cutoff was $p < 0.05$.

(F) Pseudotime analysis using Monocle-2 across naive, Cl13, and Cl13ΔCD4 P14 populations from D8 p.i. and 513 exhaustion-specific genes (ESGs) (from Bengsch et al., 2018). Predicted “Teff-like cell” and “Tex precursor cell” branches were identified in the pseudotime trajectory. Distribution of clusters 2, 3, 4, and 5 from (B) is shown.

(G) Expression of *Tcf7*, *Gzmb*, and *Havcr2* projected onto the pseudotime trajectory.

(H) Expression of *Klrg1* and a *Klrg1*⁺ *DiffGene* signature (from Herndler-Brandstetter et al., 2018) projected onto the pseudotime trajectory. Figure 1

(I) Expression of *Entpd1* and *Entpd1*⁺*Havcr2*⁺ *DiffGene* and *Tcf7*⁺*Pdcd1*⁺ *DiffGene* signatures (from Sade-Feldman et al., 2018) projected onto the pseudotime trajectory.

Also see Figure S1.

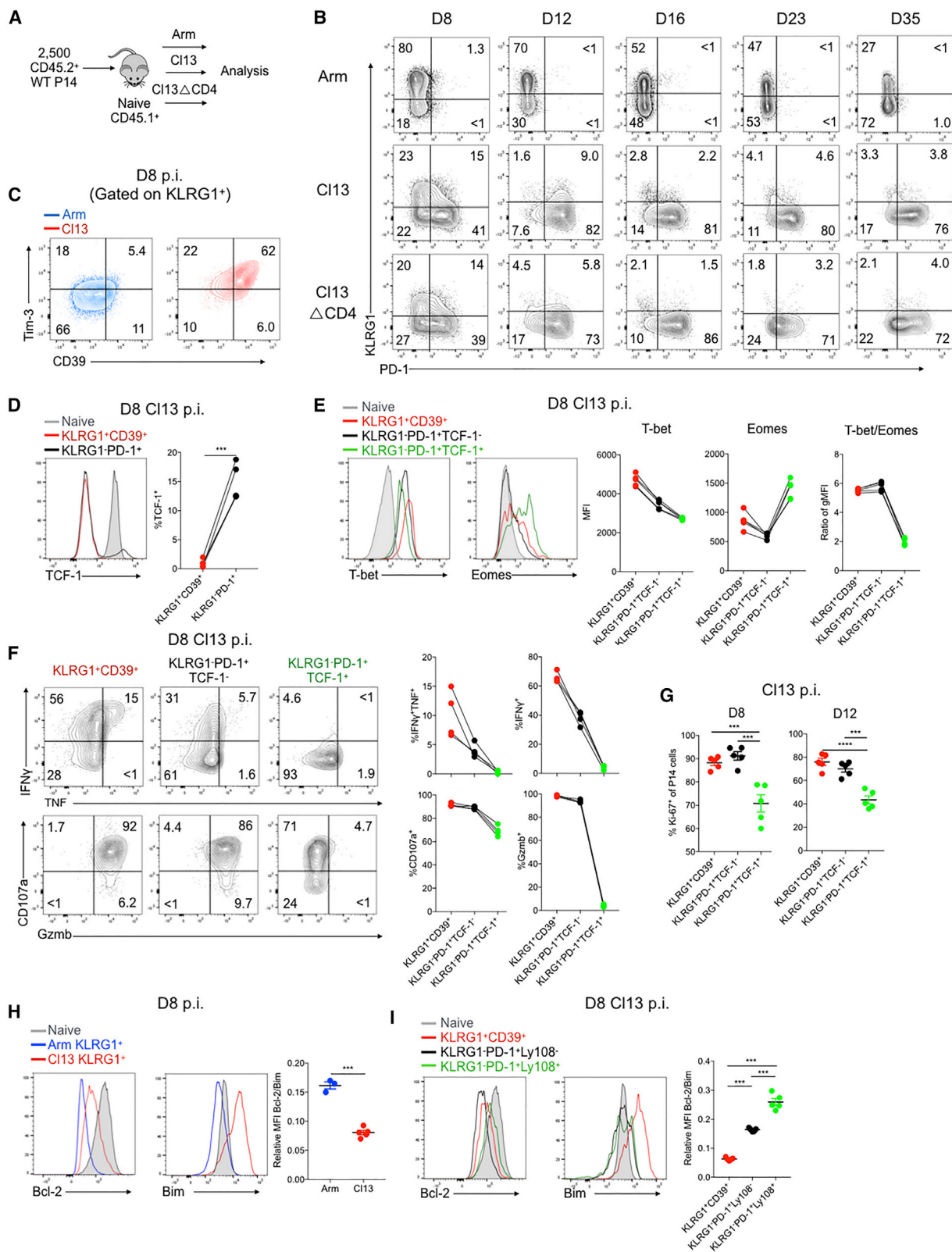


Figure 2. Distinct Cellular and Molecular Profiles of Teff-like and Tex Precursor Cells during Chronic Infection

(A) Experimental design. 2.5×10^5 CD45.2⁺ P14 cells were adoptively transferred into naive CD45.1⁺ mice and then infected with LCMV Arm, CI13, or CI13ΔCD4. Spleens were analyzed at the indicated time points.

(legend continued on next page)

1 had high expression of *Klrg1*, *Klrd1*, *Gzma*, *Gzmb*, *Id2*, and *Ccr2* (Figures 1D and S1A), in agreement with the preponderance of Arm-derived Teff cells in this cluster. This cluster also expressed *Ifng* and *Tbx21* but to a similar extent as clusters 3 and 4 (Figure 1D). Clusters 2, 3, and 4 all expressed *Pdcd1* (encoding PD-1), consistent with enrichment of the D8 Cl13 and Cl13ΔCD4 P14 cells in these clusters. However, whereas clusters 3 and 4 displayed high *Gzmb*, cluster 2 was relatively depleted of this gene. Cluster 4 was enriched with cell-cycle genes, such as *Ccnb2*, *Cks1b*, *Cenpa*, *Cdk2*, and *Mki67* (Figures 1D and S1A). Cluster 3 contained genes encoding chemokines (*Ccl3*, *Ccl4*, and *Ccl5*), *Gzmb* and other activation genes (e.g., *S100a4*, *S100a6*, *Lgals1*, and *Nkg7*), and the inhibitory receptor *Lag3* (Figures 1D and S1A). Cluster 2 was enriched with cells expressing *Cxcr5*, *Tcf7* (encoding TCF-1), and *Slamf6* (encoding Ly108) and was relatively depleted of cells expressing *Havcr2* (encoding Tim3). In addition, cluster 2 displayed expression of a subset of interferon-stimulated genes (ISGs) and transcriptional coordinators, such as *Batf*, *Id3*, *Tox*, and *Nr4a1* (Figures 1D and S1A). Cluster 1 and, to a lesser extent, cluster 3 were enriched with Gene Ontology (GO) terms reflecting cell trafficking and effector functions, whereas cluster 2 showed preferential enrichment of “response to virus,” most likely reflecting ISGs (Figure 1E). Cluster 4 had strong enrichment of cell-cycle-related GO terms, consistent with individual gene-expression data and also with the notion of ongoing proliferation during the development of exhaustion (Doering et al., 2012; Wherry et al., 2007). Cluster 2 was of particular interest given the high co-expression of *Pdcd1*, *Tcf7*, *Slamf6*, and *Bcl2* and the relative lack of *Gzmb*, *Havcr2*, and markers of the cell cycle. This cluster is reminiscent of recently described TCF-1⁺ Tex progenitor cells in established exhaustion (Im et al., 2016; Utschneider et al., 2016; Wu et al., 2016).

Developmental Bifurcation of Tex Precursor Cells and Teff-like Cells at the Early Stage of Chronic Infection

We next used these scRNA-seq data to infer predicted developmental relationships during chronic infection. We applied a list of exhaustion-specific genes (ESGs; n = 513 genes; Bengsch et al., 2018) and used Monocle-2 (Qiu et al., 2017) to perform pseudotime analysis on P14 cells from naive mice, as well as D8 Cl13 and Cl13ΔCD4 mice. These analyses revealed a trajectory originating at Tn cells but then bifurcating into two branches containing cells from early chronic infection (Figure 1F). We tentatively labeled the upper branch “Tex precursor cells” because this branch was enriched with cells from cluster 2 above (Figure 1F) and displayed high *Tcf7* expression (Figure 1G). The lower

branch we termed “Teff-like cells” because cells in this branch were enriched with cells from clusters 3 and 4 (Figure 1F) and had high expression of *Gzmb* and *Havcr2* (encoding Tim3; Figure 1G). This branch also lacked *Tcf7* (Figure 1G).

Although present across the entire dataset, *Klrg1* expression was most prominent in cluster 1, which contained the cells from D8 Arm (Figure S1A). The pseudotime branch with high *Gzmb* and *Havcr2* expression had higher *Klrg1* expression and enrichment of a KLRG1⁺ cell gene set (*Klrg1*⁺*DiffGene* generated from Herndler-Brandstetter et al., 2018) than the Tex cell precursor branch (Figures 1H and S1B). Detection among the Cl13 clusters (2, 3, and 4) was generally low (Figure S1B). However, projecting the *Klrg1*⁺*DiffGene* signature on the pseudotime trajectories revealed higher representation of this transcriptional program in the *Gzmb* and *Havcr2* branch and lower expression in the *Tcf7*⁺ branch (Figure 1H).

Recent studies have defined CD39 or CD39 with Tim-3 as a potential marker of terminal differentiation of T cells during chronic infection and cancer (Gupta et al., 2015; Sade-Feldman et al., 2018). Thus, we next examined Tim-3 (encoded by *Havcr2*) and CD39 (encoded by *Entpd1*) expression. The lower Teff-like cell branch in the pseudotime analysis from early chronic infection displayed high expression of *Havcr2* (Figure 1G) and *Entpd1* (Figure 1I). Furthermore, we generated a *Havcr2*⁺*Entpd1*⁺ *DiffGene* signature (Sade-Feldman et al., 2018). This *Havcr2*⁺*Entpd1*⁺ *DiffGene* signature was also more strongly enriched in clusters 3 and 4 than in cluster 2 (Figure S1C) and the lower Teff-like cell branch in the pseudotime analysis (Figure 1I). We also generated a *Tcf7*⁺*Pdcd1*⁺ *DiffGene* signature (Sade-Feldman et al., 2018) and found that this signature was strongly enriched in the Tex precursor cell branch (Figure 1I). Together, these data suggest that a binary developmental bifurcation early in the formation of Tex precursor cells consists of a divergence of a Teff-like cell branch and a distinct *Tcf7*⁺*Pdcd1*⁺ Tex precursor cell branch.

KLRG1⁺ Teff-like Cells from Chronic Infection Display a Molecular Signature Distinct from That of PD-1⁺ Tex Cells

We next examined the relationship between Teff cells and developing Tex cells by using flow-cytometric analysis. Thus, we examined protein expression of KLRG1 (Joshi et al., 2007) and PD-1. At D8 post-infection (p.i.) with Arm, a robust population of KLRG1⁺ Teff cells was readily apparent, as described in Joshi et al., 2007 (Figures 2A and 2B). This KLRG1⁺ population was substantially reduced at D8 p.i. with Cl13 and Cl13ΔCD4 (Figures

(B) KLRG1 and PD-1 expression at the indicated time points of Arm, Cl13, and Cl13ΔCD4 infections. Flow-cytometry plots are gated on donor P14 cells.

(C) Flow-cytometry plots for CD39 and Tim-3 by KLRG1⁺ P14 cells from Arm versus Cl13 at D8 p.i.

(D) TCF-1 expression on D8 p.i. with Cl13 in P14 cells gated on KLRG1⁺CD39⁺ or KLRG1⁺PD-1⁺ subsets. Naive CD8 T cells (endogenous CD62L⁺CD44⁻) are displayed as a control.

(E) T-bet and Eomes expression assessed at D8 p.i. with Cl13 in P14 cells gated on KLRG1⁺CD39⁺, KLRG1⁻PD-1⁺TCF-1⁻, or KLRG1⁻PD-1⁺TCF-1⁺ subsets. Naive CD8 T cells are displayed as a control. The T-bet/Eomes ratio was calculated according to geometric MFI.

(F) IFN-γ, TNF, CD107a, and Granzyme B (*Gzmb*) expression assessed at D8 p.i. with Cl13 by P14 cells gated on the indicated subsets.

(G) The percentage of Ki-67⁺ cells in the indicated subsets of P14 cells was assessed at D8 and D12 p.i. with Cl13.

(H) Bcl-2 and Bim expression were assessed at D8 p.i. with Arm in the KLRG1⁺ P14 subset. Naive CD8 T cells are displayed as a control. The Bcl-2/Bim ratio was calculated according to geometric MFI.

(I) Bcl-2 and Bim expression were assessed at D8 p.i. with Cl13 p.i. in the indicated subsets of P14 cells. Naive CD8 T cells are displayed as a control. The Bcl-2/Bim ratio was calculated according to geometric MFI.

*p < 0.05, **p < 0.01, ***p < 0.001, ****p < 0.0001 versus control (two-tailed Student's t test or one-way ANOVA). Data are representative of 2–6 independent experiments with at least 3 mice per group (mean ± SEM). Also see Figures S2 and S3.

2A, 2B, S2A, and S2B). Over the ensuing weeks, the KLRG1⁺ population gradually declined after Arm infection. In contrast, this population decreased precipitously during chronic infection such that <5% of the P14 population expressed KLRG1 by D16 p.i. (Figures 2B, S2A, and S2B). During developing chronic infection, a clear population of PD-1⁺ cells was present at D8 p.i., and these cells were KLRG1⁻ (Figures 2B, S2A, and S2B), suggesting at least partially mutually exclusive expression of KLRG1 and PD-1 in this setting. Compared with cells from Arm infection, the KLRG1⁺ cells from CI13 infection at D8 p.i. had substantially higher expression of CD39 and Tim-3 in spleen (Figure 2C) and other organs (Figures S2C and S2D), consistent with the Teff-like cell branch in the pseudotime above. A KLRG1⁺CD39⁺ population was also detectable in tumor-infiltrating lymphocytes (TILs) from CT26 tumors (Figures S2E and S2F).

At D8 p.i., the KLRG1⁺CD39⁺ cells lacked TCF-1, and TCF-1 expression was exclusively found in the KLRG1⁻PD-1⁺ population (Figure 2D). We next divided the PD-1⁺ P14 cells into TCF-1⁺ and TCF-1⁻ subpopulations and interrogated these subpopulations in more detail (Figure S2G). For example, whereas the KLRG1⁺CD39⁺ Teff-like cell population from chronic infection expressed the highest T-bet, expression of this TF was higher in PD-1⁺TCF-1⁻ than in PD-1⁺TCF-1⁺ cells (Figure 2E). In contrast, Eomes was the highest in the PD-1⁺TCF-1⁺ D8 P14 population but lower in both the PD-1⁺TCF-1⁻ and KLRG1⁺CD39⁺ populations. Furthermore, the T-bet/Eomes ratio was lowest in the PD-1⁺TCF-1⁺ population (Figure 2E). As expected, the KLRG1⁺CD39⁺ P14 cells displayed robust effector functions (Figure 2F). Between the two PD-1⁺ subpopulations, the PD-1⁺TCF-1⁺ cells were the least efficient at elaborating cytokines, expressing granzyme B, or degranulating (Figure 2F). A similar hierarchy was observed when *in vivo* proliferation was examined at D8 or D12 p.i. in that the PD-1⁺TCF-1⁺ cells displayed the lowest Ki67 expression (Figure 2G).

KLRG1⁺ P14 cells generated early during chronic infection fail to persist long term (Angelosanto et al., 2012). Thus, we examined expression of the anti- and pro-apoptotic molecules Bcl-2 and Bim. The KLRG1⁺ P14 population at D8 p.i. with CI13 had higher expression of both Bcl-2 and Bim than the KLRG1⁺ T_{EFF} cells from Arm infection (Figure 2H). However, the KLRG1⁺ population from Arm infection had a substantially higher Bcl-2/Bim ratio (Figure 2H). Moreover, the KLRG1⁻PD-1⁺ subsets from D8 p.i. with CI13 had a considerably higher Bcl2/Bim ratio than the KLRG1⁺CD39⁺ cells (Figure 2I). Among the KLRG1⁻PD-1⁺ cells from CI13 infection, the subpopulation that expressed TCF-1⁺ (with Ly108 as a surrogate; Figure S2H) had the highest Bcl-2/Bim ratio among the subsets at D8 of CI13 infection (Figure 2I). These patterns of TF expression, effector function, proliferation, and pro- and anti-apoptotic molecule expression were also observed in the CI13ΔCD4 setting (Figure S3).

The low Bcl-2/Bim ratio in the KLRG1⁺ CD8 T cells from CI13 infection suggests that these cells might be more prone to cell death. Thus, we examined genome integrity by using DAPI and gH2AX staining to identify cells with stable chromatin and nuclear structure, nuclear envelope blebbing, and nuclear lamina de-association indicating pre-apoptosis or apoptotic cells with complete co-staining of DAPI and nuclear lamina γH2AX (Figure S2I). At D8 p.i. with CI13, KLRG1⁺CD39⁺ virus-specific CD8 T cells had the highest proportion of apoptotic and pre-

apoptotic cells, and KLRG1⁻PD-1⁺Ly108⁻ (i.e., TCF-1⁻) cells had the second highest. In contrast, the KLRG1⁻PD-1⁺Ly108⁺ (i.e., TCF-1⁺) subset had the highest proportion of non-apoptotic nuclei (Figure S2I). Together, these data suggest that KLRG1⁺ Teff-like cells found at the early stage of chronic infection are highly susceptible to cell death, consistent with the inability of these cells to persist long term *in vivo*.

Compared with PD-1⁺ Tex Cells, KLRG1⁺ Teff-like Cells Persist Poorly during Chronic Viral Infection

To define the developmental relationship between the subsets described above, we conducted lineage-tracing experiments. We sorted KLRG1⁺CD39⁺, KLRG1⁻PD-1⁺Ly108⁻, and KLRG1⁻PD-1⁺Ly108⁺ cells at D7 or D8 p.i. and adoptively transferred equal numbers of each subset into congenically distinct, infection-matched recipient mice (Figures 3A and S4D). At D8 post-transfer (p.t.), progeny of KLRG1⁻PD-1⁺Ly108⁺ Tex precursor cells were considerably more numerous than cells derived from KLRG1⁺CD39⁺ or KLRG1⁻PD-1⁺Ly108⁻ donor populations (Figure 3B), consistent with TCF-1 expression by this PD-1⁺Ly108⁺ subset (Utzschneider et al., 2016). However, when we compared the two D8 subsets that lacked TCF-1 expression, the KLRG1⁻PD-1⁺Ly108⁻ population persisted significantly better than the KLRG1⁺CD39⁺ Teff-like cell population (Figure 3B). We also analyzed changes in differentiation state. Although both KLRG1⁻ donor populations maintained high PD-1 expression (Figures S4A and S4B), neither of these subsets gave rise to appreciable numbers of KLRG1⁺ cells in this setting (Figures 3C and S4C). These data suggest that divergent fate commitment to Tex precursor cells versus KLRG1⁺ Teff cells had occurred prior to formation of the KLRG1⁻PD-1⁺Ly108⁻ and KLRG1⁻PD-1⁺Ly108⁺ populations or that development of KLRG1⁺ cells was antagonized by D8 of chronic infection. Moreover, PD-1⁺Ly108⁺ cells were able to generate PD-1⁺Ly108⁻ cells, whereas the opposite was inefficient (Figures 3C and S4C). These developmental relationships were also observed for non-P14 D^bGP33 tetramer⁺ CD8 T cells (Figures S4D–S4F). Thus, these lineage-tracing experiments highlight a major difference in durability of the three D8 virus-specific CD8 T cell populations generated during CI13 infection and suggest that Tex precursor cells are distinct from KLRG1⁺ Teff-like cells.

TCF-1 Represses the Teff-like Cell Fate in Early Chronic Infection and Fosters Establishment of a Tex Cell Population

Recent studies have identified a key role for TCF-1 in established exhaustion where genetic deletion of TCF-1 results in the loss of Tex cells, specifically during the post-effector phase (Im et al., 2016; Utzschneider et al., 2016; Wu et al., 2016), suggesting a role for TCF-1 in the transition from the effector phase to exhaustion. However, how and when this TCF-1-dependent activity occurs is unclear. To investigate this question, we co-transferred equal numbers of congenically distinct wild-type (WT) (*Tcf7*^{fllox/fllox}*xCd4*^{WT}) and *Tcf7*^{fllox/fllox}*xCd4*^{CRE} P14 cells to recipient mice of a third congenic background and then infected the mice with CI13 (Figure 4A). *Tcf7*^{fllox/fllox}*xCd4*^{CRE} P14 cells mounted an initial response but failed to seed a durable Tex cell pool (Figure 4B), as expected (Im et al., 2016; Utzschneider et al., 2016; Wu et al.,

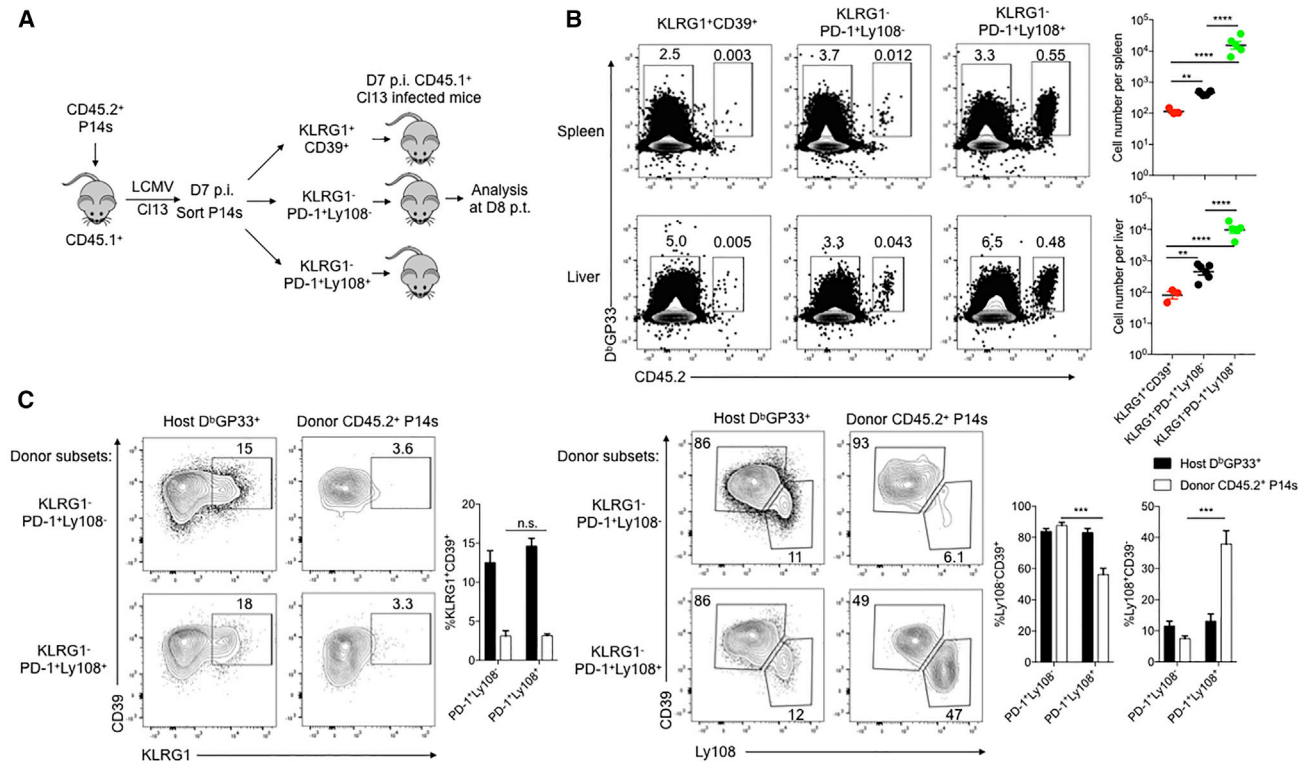


Figure 3. Lineage Tracing of Subpopulations of Teff-like and Tex Precursor Cells in Early Chronic Viral Infection

(A) Experimental design. 5×10^3 CD45.2⁺ P14 cells were adoptively transferred into naive CD45.1⁺ C57BL/6 recipient mice and then infected with CI13 1 day later. On D7 p.i., KLRG1⁺CD39⁺, KLRG1⁻PD-1⁺Ly108⁻, or KLRG1⁻PD-1⁺Ly108⁺ P14 CD8 T cells were isolated, and 3×10^5 of each were adoptively transferred into infection-matched CD45.1⁺ recipient mice. Donor P14 cells were analyzed on D8 p.i.

(B) Flow-cytometry plots and quantification of donor CD45.2⁺ D^bGP33 tetramer⁺ P14 cells derived from the indicated subsets. Endogenous CD45.2⁻ D^bGP33 tetramer⁺ CD8 T cells are shown as controls.

(C) Flow-cytometry plots and quantification of splenic CD45.2⁺ donor P14 cells and host D^bGP33 tetramer⁺ cells that are KLRG1⁺, Ly108⁻CD39⁺, or Ly108⁺CD39⁻. Note that there were too few KLRG1⁺CD39⁺ P14 cells for analysis on D8 p.i. (see B).

* $p < 0.05$, ** $p < 0.01$, *** $p < 0.001$, **** $p < 0.0001$ versus control (two-tailed Student's *t* test or one-way ANOVA). Data representative of at least 3 mice per group (mean \pm SEM). Also see Figure S4.

2016). On the basis of the scRNA-seq detailed earlier, we next examined whether the distribution of cells corresponding to the Teff-like versus Tex precursor cell branches identified in the pseudotime analysis was altered in the absence of TCF-1. Indeed, staining for markers of these two pseudotime-defined branches revealed a substantial shift in the absence of TCF-1: there were fewer KLRG1⁻PD-1⁺ P14 cells and a substantially higher proportion of KLRG1⁺CD39⁺ or Tim-3⁺CD39⁺ P14 than observed for WT P14 cells in CI13 infection (Figures 4C and 4D).

We next investigated how enforced TCF-1 expression affects early population dynamics. The p45 isoform has a β -catenin binding domain (Ioannidis et al., 2001) that could influence function (Anastas and Moon, 2013), whereas the p33 isoform lacks this domain. Thus, we expressed TCF-1 p33 or TCF-1 p45 in P14 cells *in vivo* by using retrovirus (RV) expression (Figures 4E and S5A) as previously described (Kurachi et al., 2017). RV expression of either TCF-1 isoform repressed the formation of KLRG1⁺CD39⁺ or Tim-3⁺CD39⁺ P14 cells at D8 p.i. with CI13. Moreover, enforced expression of either TCF-1 p33 or TCF-1 p45 increased the proportion of Ly108⁺CD39⁻ P14 cells upon infection (Figure 4F). As chronic infection progressed, the p33

isoform displayed stronger repression of KLRG1 or CD39 expression (Figure S5B), whereas the p45 isoform more efficiently promoted CD127 and CXCR5 expression (Figures 4G and S5B). Both TCF-1 isoforms also promoted PD-1 expression (Figure 4G) at D15, a time point corresponding to the developmental transition between the effector phase and early establishment of exhaustion (Angelosanto et al., 2012; Crawford et al., 2014; Doering et al., 2012; Schietinger et al., 2016). Moreover, the p45 isoform appeared to more efficiently foster durability of the Tex cell population in established chronic infection (Figures S5C–S5F). A similar effect of TCF-1 expression was observed in the Δ CD4 setting (Figures S5G and S5H). Together, these data underscore the importance of TCF-1 in T cell exhaustion. However, these experiments also further reveal a major role for TCF-1 in repressing the more terminal Teff-like cell branch early during the development of exhaustion.

PD-1 Supports Development of the TCF-1⁺ Tex Precursor Cell Population Early during Chronic Infection

High expression of PD-1 is emblematic of terminal Tex cells, whereas intermediate PD-1 is expressed by the progenitor Tex

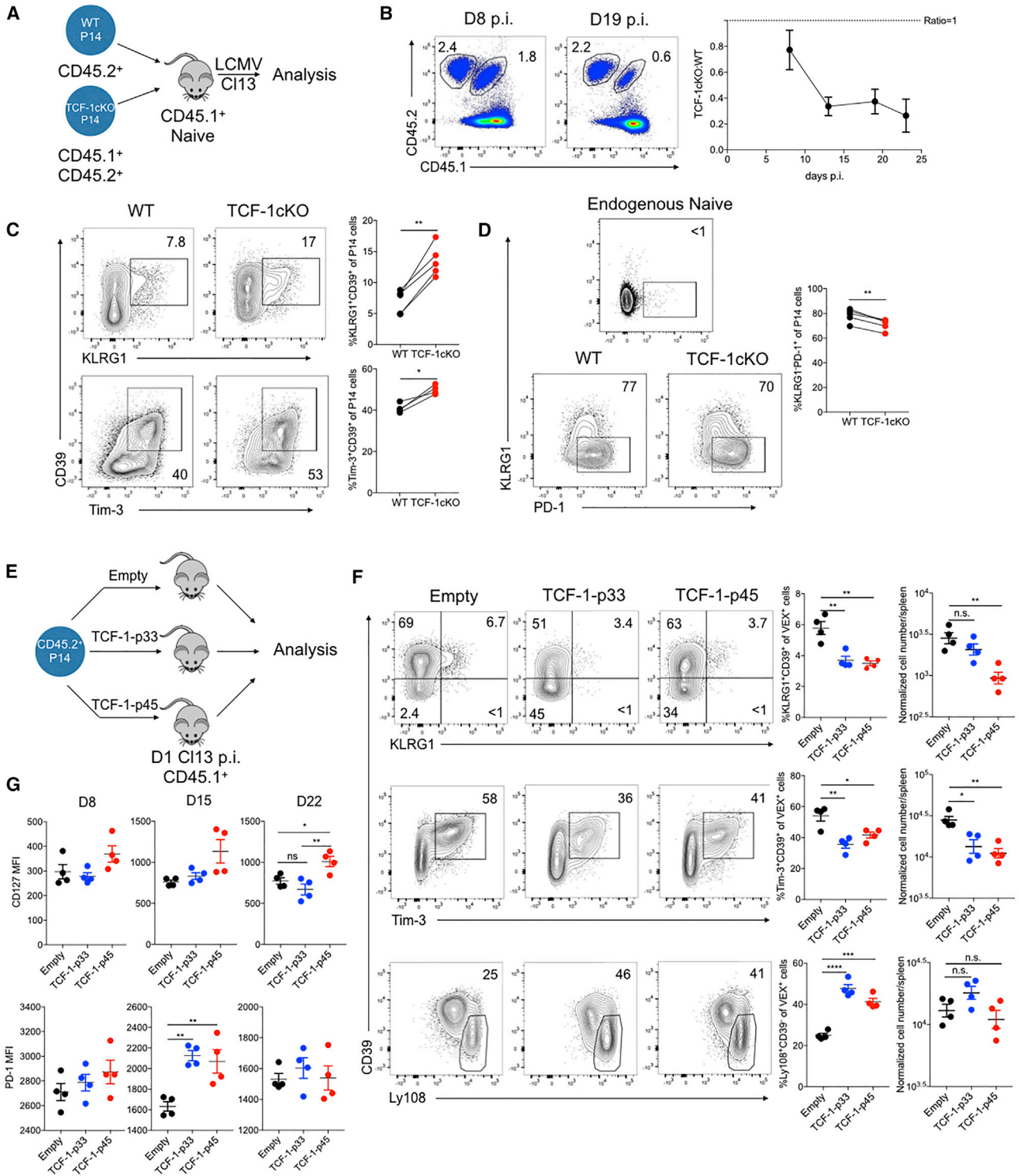


Figure 4. TCF-1 Regulates the Early Fate Bifurcation between Teff-like and Tex Precursor Cells

(A) Experimental design. 1×10^3 CD45.2⁺ *Tcf7*^{fllox/fllox}*x**Cd4*^{WT} (WT) littermate control P14 CD8 T cells and 1×10^3 CD45.1⁺CD45.2⁺ *Tcf7*^{fllox/fllox}*x**Cd4*^{CRE} (TCF-1cKO) P14 CD8 T cells were co-transferred into CD45.1⁺ naive recipient mice and then infected with CI13. Splenocytes were isolated on the indicated days p.i. for analysis.

(B) Flow-cytometry plots quantifying WT and TCF-1cKO P14 cells. The ratio of cells is plotted over time p.i.

(C) Flow-cytometry plots and quantification of KLRG1⁺CD39⁺ and Tim-3⁺CD39⁺ subsets of responding P14 cells of each genotype on D8 p.i. with CI13.

(legend continued on next page)

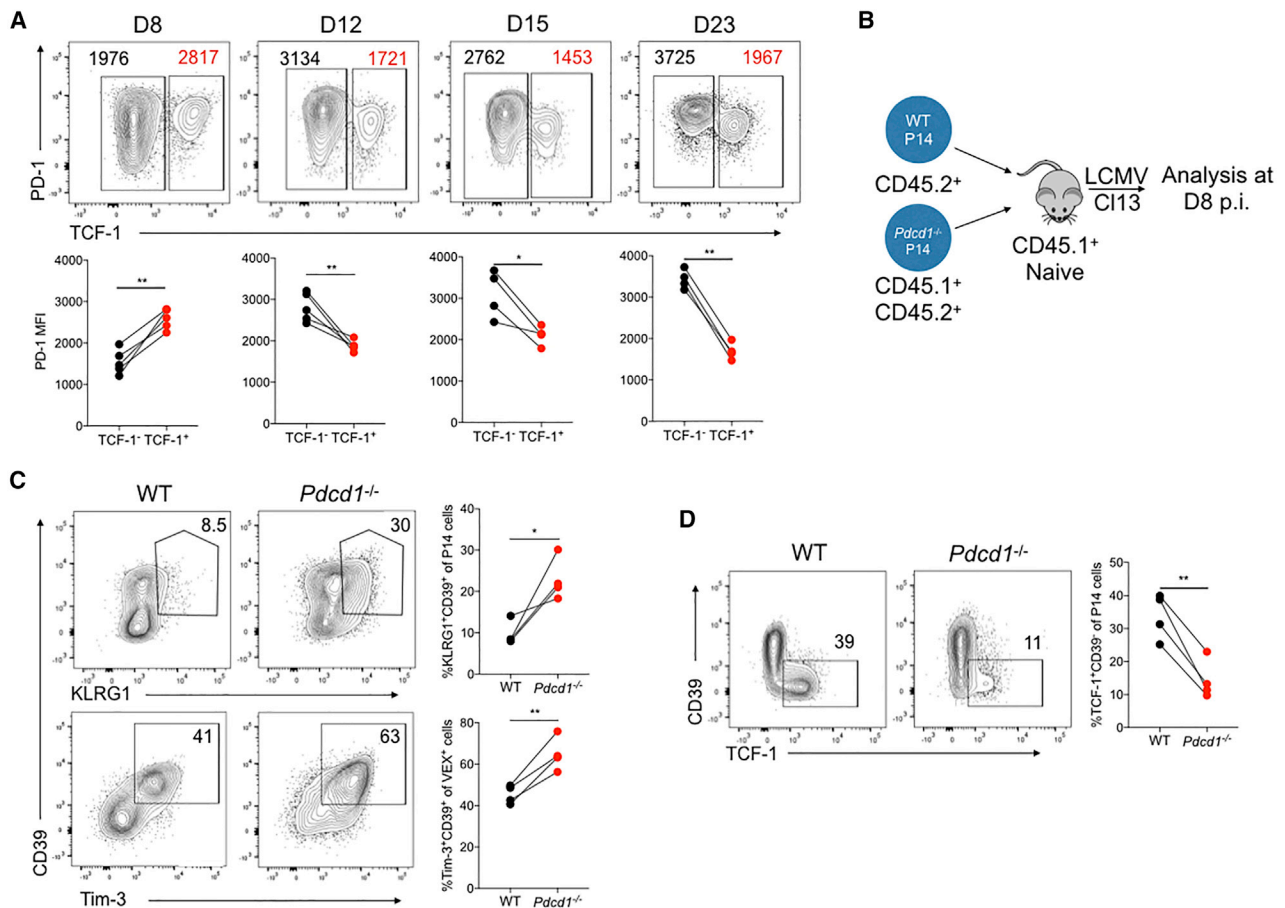


Figure 5. PD-1 Maintains the TCF-1⁺ Tex Precursor Cell Population at the Early Stage of Chronic Infection

(A) Flow-cytometry plots of TCF-1 and PD-1 expression by responding P14 cells at the indicated days of CI13 infection. PD-1 MFI of TCF-1⁻ (black) and TCF-1⁺ (red) subsets of P14 cells is shown in the flow-cytometry plots and summary data.

(B) Experimental design. 5×10^2 CD45.2⁺ WT P14 and 5×10^2 CD45.1⁺CD45.2⁺ *Pdcd1*^{-/-} P14 cells were co-adoptively transferred into CD45.1⁺ naive recipient mice and then infected with CI13. Responding P14 cells from the spleen were analyzed on D8 p.i. with CI13.

(C) Flow-cytometry plots and quantification of KLRG1⁺CD39⁺ or Tim-3⁺CD39⁺ subsets of responding WT or *Pdcd1*^{-/-} P14 cells on D8 p.i.

(D) Flow-cytometry plots and quantification of TCF-1⁺CD39⁻ subsets of responding WT or *Pdcd1*^{-/-} P14 cells on D8 p.i.

* $p < 0.05$, ** $p < 0.01$ versus control (two-tailed Student's *t* test). Data are representative of 2–4 independent experiments (mean \pm SEM) with at least 3 mice per group. Also see Figure S6.

cell population (Blackburn et al., 2008). In the established Tex cell pool, the expression of PD-1 is negatively correlated with TCF-1 (Im et al., 2016), in contrast to the high *Pdcd1* expression in the *Tcf7* cluster as revealed by the sc-RNA-seq detailed earlier (Figures 1D and S1A). Indeed, in established chronic infection, the TCF-1⁺ Tex cell population had lower PD-1 expression than the TCF-1⁻ subset (Figure 5A), though this amount of

PD-1 was still higher than that expressed by Tmem cells (data not shown). In contrast, in early chronic infection (D8 p.i.), TCF-1⁺ P14 cells expressed high PD-1 (Figure 5A). This contrasts with D8 Arm, where PD-1 expression is already low (Barber et al., 2006; Wherry et al., 2007). Thus, we next tested whether PD-1 has a role in these CD8 T cell subsets in early chronic infection. Congenically distinct *Pdcd1*^{-/-} and WT P14 cells

(D) Flow-cytometry plots and quantification of the KLRG1⁺PD-1⁺ subset of responding P14 cells of each genotype on D8 p.i. with CI13. Endogenous naive CD8 T cells are used for controls.

(E) Experimental design. WT P14 CD8 T cells transduced with the indicated RVs were adoptively transferred into mice infected 1 day previously with CI13. Donor RV reporter⁺ (VEX⁺) P14 cells were analyzed at the indicated time points.

(F) Flow-cytometry plots and quantification of the indicated P14 cell subsets for the indicated RV groups on D8 p.i. with CI13 p.i. Plots are gated on VEX⁺ P14 cells. VEX⁺ cell numbers were normalized to 1×10^4 VEX⁺P14 cell engraftment according to the transduction efficiency on D2 p.i.

(G) Quantification of CD127 and PD-1 expression by P14 cells transduced with the indicated RVs at the indicated time points of CI13 infection.

* $p < 0.05$, ** $p < 0.01$, *** $p < 0.001$, **** $p < 0.0001$ versus control (two-tailed Student's *t* test). Data are representative of 3–4 independent experiments (mean \pm SEM) with at least 4 mice per group. Also see Figure S5.

were co-adoptively transferred and then infected with CI13 (Figure 5B) as previously described (Odorizzi et al., 2015). This approach revealed a substantial increase in KLRG1⁺CD39⁺ or Tim-3⁺CD39⁺ cells (Figure 5C) and reduction in the TCF-1⁺ subset at D8 p.i. in the absence of PD-1 (Figures 5D, S6A, and S6B). These data are consistent with the observation that the absence of PD-1 results in the erosion of the Tex cell population over time (Odorizzi et al., 2015). Thus, PD-1 is important to preserve the TCF-1⁺ Tex precursor cell population and repress the formation of the terminal Teff-like cell subset in early chronic infection.

State Transition Inference Prediction Identifies Transcriptional Circuits Downstream of TCF-1 in Tex Cells

To begin to understand how TCF-1 might be involved in early events of the establishment of CD8 T cell exhaustion, we developed a computational approach for inferring transcriptional circuits. This approach uses a selected pseudotime trajectory, anchors on a TF of interest (in this case *Tcf7*), and then correlates expression of other transcriptional regulators with *Tcf7* across the pseudotime trajectory. Thus, sets of TFs that are correlated and anti-correlated with *Tcf7*, as well as those key TFs that change dynamically specifically at the major inflection point of change in *Tcf7* expression, are identified. Using scRNA-seq data, this latter feature can reveal transcriptional circuits working coordinately or in opposition specifically at transitions between cell states. One advantage of this approach, termed state transition inference predictor (STIP), is that it overcomes some limitations of lowly expressed genes by using correlation coefficients rather than absolute gene expression (see STAR Methods). Thus, applying STIP to the data above showed *Tcf7* expression to undergo a monotone increase, allowing anchoring on this gene for analysis (Figure 6A). Several TF genes, including *Tox*, *Id3*, *Eomes*, *Myb*, and *Nr4a1*, were positively correlated with *Tcf7* (Figure 6B). In contrast, *Id2* was strongly anti-correlated with *Tcf7*. We then examined an extended list of TFs (Figure 6C). Two major clusters of TFs emerged, including one that contained *Id3*, *Eomes*, *Myb*, *Batf*, *Irf4*, *Tox*, *Nr4a1*, and *Hif1a* and was positively correlated with *Tcf7* over the pseudotime trajectory and a second cluster that contained *Id2*, *Runx1*, *Prdm1*, *Tbx21*, *Irf1*, and *Irf8* and was negatively correlated with *Tcf7*. In addition to these two major clusters, several TF genes, including *Smad7*, *Gata3*, *Runx2*, and *Zeb2*, occupied an intermediate location in the pseudotime trajectory around the point of greatest change for *Tcf7* and *Id2*, perhaps reflecting a metastable state or additional (perhaps transient) population heterogeneity (Figure 6C).

To further interrogate how TCF-1 might regulate the TFs identified by STIPs in Tex cells, we constructed a transcriptional network (Figure 6D). We used existing ATAC-seq (assay for transposase accessible chromatin using sequencing) data (Sen et al., 2016) and identified TF-encoding genes containing a predicted TCF-1 motif in open chromatin regions. We identified TFs predicted to be regulated by TCF-1 in Tn cells only (e.g., *Ikzf1* and *Gata3*), in Tn cells and early Tex precursor cell populations (e.g., *Myb*, *Hif1a*, *Eomes*, *Id3*, and *Prdm1*), or only in early Tex precursor cell populations (e.g., *Id2*, *Tox*, *Zeb2*, *Smad7*, *Batf*, and *Nfatc1*) (Figure 6D). Notably, TCF-1 was predicted to repress genes that are involved in Teff cell differentiation (including *Id2*, *Prdm1*, and *Runx1*) and to promote expression of genes that

have been implicated in fostering exhaustion (such as *Eomes*, *Batf*, and *Nfatc1*) (Figure 6D). TCF-1 might also have a more complex regulatory connection to *Smad7* and *Zeb2* because the greatest change in expression of these genes occurred at the transition of greatest change in *Tcf7* (Figures 6C and 6D). Thus, these data suggest a key role for TCF-1 in coordinating transcriptional circuitry at time points corresponding to the formation of precursors of Tex cells.

TCF-1 Mediates a T-bet and Eomes Transition during Chronic Infection

Previous studies identified roles for T-bet and Eomes in progenitor and terminal Tex cell subsets (Paley et al., 2012), and genetic deletion of T-bet, Eomes, or TCF-1 results in a collapse of the mature Tex cell population (Im et al., 2016; Paley et al., 2012; Utschneider et al., 2016). However, the relationship between these three TFs remains to be defined. According to the data above and a known connection between TCF-1 and Eomes in Tmem cells (Zhou et al., 2010), we hypothesize that TCF-1 might regulate T-bet and/or Eomes in developing Tex precursor cells. At D8 of chronic infection, a subpopulation of TCF-1⁺ virus-specific CD8 T cells that expressed Eomes was identifiable (Figure 7A). Moreover, these TCF-1⁺ Tex precursor cells expressed slightly lower T-bet than the TCF-1⁻ population (Figures 7A and 2E). Similar patterns were observed for tumor-infiltrating CD8 T cells at D8 in mouse CT26 tumors (Figure 7B). Genetic deletion of TCF-1 reduced Eomes expression at D8 of CI13 infection (Figure 7C). In contrast, although the percentage of T-bet⁺ cells decreased, the amount of T-bet per cell mean fluorescence intensity (MFI) was moderately increased in the absence of TCF-1 (Figure 7C). These data suggest that TCF-1 was upstream of Eomes but had only a minimal effect on T-bet at this time point. Indeed, enforced TCF-1 expression, and in particular TCF-1 p45, promoted increasing *Eomes*^{GFP} expression and also fostered increased *Eomes* mRNA expression (Figures 7D–7F and S7A).

To further interrogate the role of Eomes in Tex cells, we crossed *Eomes*^{WT} or *Eomes*^{flox/flox} mice to CRE^{ERT2} P14 mice on a Rosa26^{L^{SL}-YFP} reporter background. We used *Eomes*^{WT} x CRE^{ERT2} x Rosa26^{L^{SL}-YFP} (Eomes WT) and *Eomes*^{flox/flox} x CRE^{ERT2} x Rosa26^{L^{SL}-YFP} inducible conditional deletion of *Eomes* on different congenic backgrounds in a co-adoptive-transfer experimental design. We then induced Eomes deletion by using tamoxifen treatment from D9 to D13 p.i. (Figure S7B). Prior to tamoxifen treatment, *Eomes*^{WT} x CRE^{ERT2} x Rosa26^{L^{SL}-YFP} or *Eomes*^{flox/flox} x CRE^{ERT2} x Rosa26^{L^{SL}-YFP} P14 cells were present at a 1/1 ratio (Figure S7C). After tamoxifen delivery, there was efficient CRE activity, as indicated by the Rosa locus YFP reporter (Figure S7D). However, 98%+ of the YFP⁺ cells were from the WT donor cells, and almost no *Eomes* inducibly deleted P14 cells survived after tamoxifen treatment (Figure S7E). These data are consistent with our previous studies demonstrating that constitutive deletion of *Eomes* compromises the development of Tex cells (Paley et al., 2012) but extend this earlier work to indicate that even after establishment of Tex precursor cells, Eomes has a critical role in the durability of this cell type. Moreover, these data indicate that a likely essential function of TCF-1 in Tex precursor cells is to mediate Eomes expression.

We next examined the role of T-bet. RV-mediated T-bet expression fostered development of KLRG1⁺CD39⁺ Teff-like

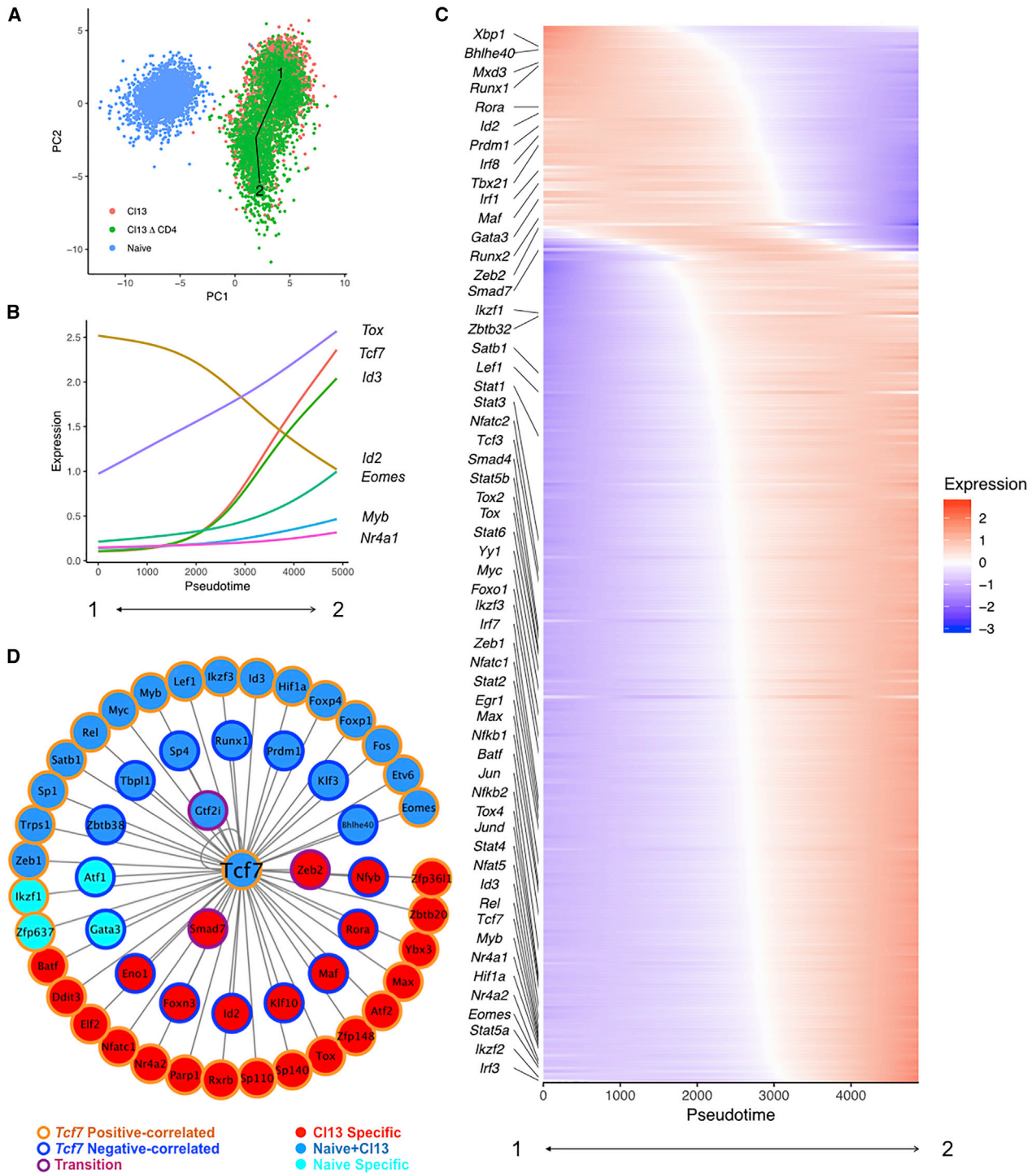


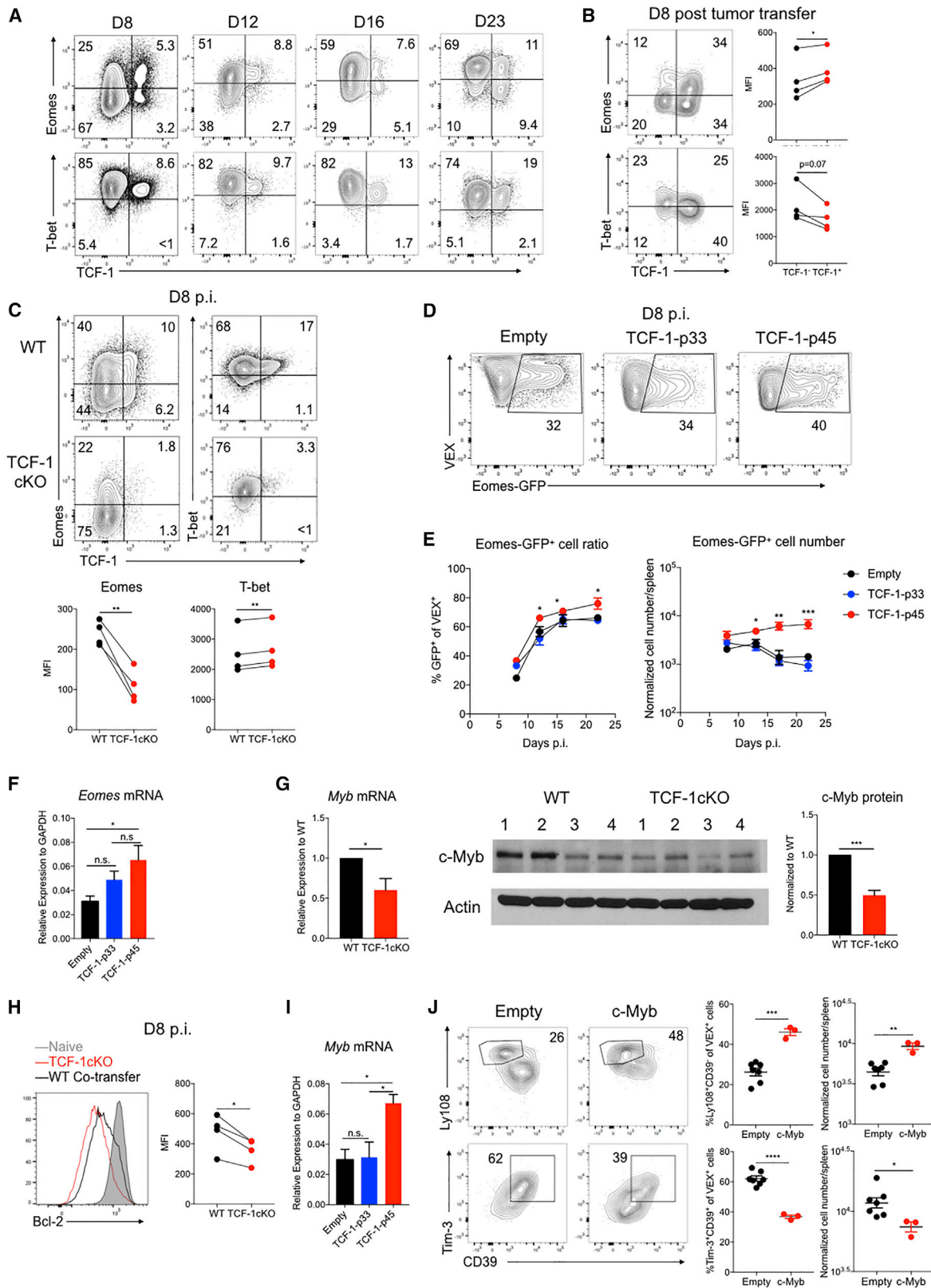
Figure 6. STIP Identifies Transcriptional Circuits Downstream of TCF-1

(A) Pseudotime trajectory across naive P14 cells and P14 cells from D8 of Cl13 and Cl13 Δ CD4 infections. PCA space was created with the ESGs from Figure 1. The line represents the longest lineage trajectory predicted by TSCAN (Ji and Ji, 2016).

(B) Expression of *Tcf7* and other indicated TFs is plotted over pseudotime.

(C) A heatmap displaying TF expression across the pseudotime trajectory.

(D) A *Tcf7*-centered network was generated (see STAR Methods). Border color for each gene represents the mRNA-expression relationship with *Tcf7* (e.g., positively [orange] or negatively [blue] correlated with *Tcf7* or neither [purple]). Fill color indicates the presence of *Tcf7* binding motif(s) in the open chromatin of the indicated TFs in naive only (cyan), naive and Cl13 (dark blue), or Cl13 only (red).



(legend on next page)

cells at D8 of CI13 infection, though the Ly108⁺CD39⁻ Tex precursor cell population was unchanged (Figure S7F). RV-enforced expression of T-bet decreased expression of PD-1, Lag-3, and CD127 at this time point but promoted expression of Tim-3 (Figure S7G), consistent with previous studies (Kao et al., 2011). Thus, during the early phases of establishing Tex cells, T-bet can promote Teff cell differentiation, consistent with the role of this TF in acute infection (Joshi et al., 2007).

TCF-1 Enhances Bcl-2 Expression via c-Myb in Tex Cells during Chronic Infection

In Tmem cells, c-Myb regulates Bcl-2 expression and promotes Tmem cell survival (Chen et al., 2017). To test whether c-Myb might also have a role in Tex cells and to test a role for TCF-1, we used the *Tcf7^{flox/flox} × Cd4^{CRE}* versus *Tcf7^{flox/flox} × Cd4^{WT}* P14 co-transfer model. In this setting, c-Myb mRNA and protein were reduced in the absence of TCF-1 at D8 of CI13 infection (Figure 7G). This reduced c-Myb expression corresponded to decreased Bcl-2 expression in the absence of *Tcf7* (Figure 7H). Conversely, *Myb* mRNA expression was induced by the p45 but not the p33 isoform of TCF-1 (Figure 7I). Furthermore, RV-expressed c-Myb significantly increased the proportion of the Tex precursor cells (Ly108⁺CD39⁻) and reduced expression of CD39 and Tim-3 (Figure 7J), suggesting that c-Myb antagonized the Teff-like cell branch of differentiation and fostered the establishment of Tex precursor cell population. Although overall cell numbers were not changed with enforced c-Myb expression (Figures S7H and S7I), there was a bias to fostering the Ly108⁺CD39⁻ subset at the expense of the Tim-3⁺CD39⁺ subset (Figure S7I). Thus, these data identify an early fate bifurcation in the establishment of the Tex precursor cell population and point to a TCF-1-related transcriptional network and TCF-1 as a key regulator necessary to antagonize an early Teff-like cell population during chronic infection and support the Tex cell developmental path.

DISCUSSION

In established Tex cells, the population dynamics and roles of specific TFs are beginning to be defined. However, the early events that form precursors of Tex cells and the relationship between these Tex precursor cells and other effector-phase populations have remained poorly understood. We addressed this question and identified a fate bifurcation that distinguished early Tex precursor cells from Teff-like cells that are generated during chronic infection. Moreover, we demonstrated that the Teff-like cell population in early chronic infection was more activated than the corresponding Teff-like cell population during acute infection and survived poorly. These studies also defined TCF-1-centered transcriptional circuits that repressed the Teff-like cell developmental path and fostered the formation of Tex precursor cells. These data are analogous to roles of TCF-1 in repressing terminally differentiated cells in other settings (Lin et al., 2015; 2016). However, our current data extend this role for TCF-1 to the setting of early chronic infection and initiation of T cell exhaustion. PD-1 plays a critical role at this stage of Tex cell development by protecting the TCF-1⁺ Tex precursor cells and ensuring that these cells can seed the long-term Tex cell pool. Moreover, we identified downstream TFs, including Eomes and c-Myb, through which TCF-1 acted in this early development of Tex precursor cells.

The strong co-expression of TCF-1 and PD-1 at D8 of chronic infection contrasts with the relationship between PD-1 and TCF-1 in established Tex cells. Our studies indicate that PD-1 is required for preserving the TCF-1⁺ Tex precursor cell population at this early time point. One possible mechanism for this early connection between PD-1 and TCF-1 is attenuation of TCR and/or CD28 signaling by PD-1 (Adams et al., 2016; Kamphorst et al., 2017; Lin et al., 2015) to prevent loss of TCF-1 expression. Another possibility is that TFs downstream of PD-1

Figure 7. TCF-1 Regulates Distinct Molecular Modules during Tex Cell Development

- (A) Flow-cytometry plots of TCF-1 and Eomes or TCF-1 and T-bet co-expression in P14 CD8 T cells on the indicated days of CI13 infection. Quadrant gates were set according to CD44⁻-naive T cells (T-bet⁻Eomes⁻TCF-1⁺) for each time point.
- (B) Flow-cytometry plots of TCF-1 and Eomes or TCF-1 and T-bet co-expression in tumor-infiltrating CD44⁺CD8 T cells (TILs) at D8 after CT26 tumor inoculation. Quadrant gates were set according to CD62L⁺CD44⁻ naive T cells (T-bet⁻Eomes⁻TCF-1⁺) from spleen. Quantification of T-bet and Eomes MFI of TCF-1⁺ or TCF-1⁻ TILs is shown on the right.
- (C) Flow-cytometry plots and quantification of Eomes and T-bet expression in WT or TCF-1cKO P14 cells at D8 p.i. with CI13.
- (D) Flow-cytometry plots of GFP expression from *Eomes^{GFP}* reporter P14 cells transduced within empty, TCF-1-p33, or TCF-1-p45 RVs on D8 p.i. with CI13. Plots are gated on VEX⁺ P14 cells (see Figure S7A for gating).
- (E) Quantification of Eomes-GFP⁺ cells in the RV-transduced P14 donor population (VEX⁺) for the indicated RV constructs on the indicated days p.i. Both percentages and numbers are shown. Cell numbers are normalized to 1 × 10⁴ VEX⁺ P14 cell engraftment according to VEX⁺ transduction efficiency on D2 p.i. (Figure S7A).
- (F) *Eomes* mRNA expression is shown for P14 cells transduced with empty, TCF-1-p33, or TCF-1-p45 RVs. VEX⁺ (i.e., transduced) P14 cells were sorted by flow cytometry on D8 CI13 p.i., and *Eomes* mRNA was measured by qRT-PCR.
- (G) *Myb* mRNA and c-Myb protein expression were examined by qRT-PCR and western blot in purified WT and TCF-1 cKO P14 cells isolated from spleens of co-transferred mice on D8 p.i. with CI13.
- (H) Flow-cytometry plots and quantification of Bcl-2 expression in WT versus TCF-1 cKO P14 cells on D8 p.i. with CI13. Histograms are gated on donor P14 cells of each genotype. Naive control is gated on endogenous CD44⁻CD8 T cells.
- (I) *Myb* mRNA expression in sorted WT P14 cells transduced with empty, TCF-1-p33, or TCF-1-p45 RVs on D8 p.i. with CI13. Transduced cells were sorted according to VEX expression.
- (J) Flow-cytometry plots and quantification of Ly108⁺CD39⁻ and Tim-3⁺CD39⁺ subsets of responding P14 cells transduced with empty versus c-Myb RVs. Plots are gated on transduced (VEX⁺) donor P14 cells on D8 p.i. with CI13. VEX⁺ cell numbers were normalized to 1 × 10⁴ VEX⁺ P14 cell engraftment according to the transduction efficiency on D2 p.i.

*p < 0.05, **p < 0.01, ***p < 0.001, ****p < 0.001 versus control (two-tailed Student's t test and one-way ANOVA analysis). Data are representative of 2 independent experiments (mean ± SEM) with at least 3 mice per group. Also see Figure S7.

could influence TCF-1 expression. Previous studies have identified BATF downstream of PD-1 (Quigley et al., 2010), and BATF was positively correlated with TCF-1 in the STIP analysis. However, the same analysis predicts that BATF might also be downstream of TCF-1 in Tex precursor cells. Thus, it is possible that a PD-1-BATF-TCF-1 feedback circuit exists in the Tex precursor cell pool. How such a circuit would be related to the Teff-cell-promoting role of BATF at early times after T cell activation (Kurachi et al., 2014) remains unclear.

Recent studies have identified Tox as a factor that progressively programs the epigenetic landscape of Tex cells over the first several weeks of chronic antigen stimulation (Alfei et al., 2019; Khan et al., 2019; Scott et al., 2019; Seo et al., 2019; Yao et al., 2019). In this context, our data suggest the following model. Early, during the first 1–2 weeks of infection or chronic antigen exposure, TF-like T-bet, Id2, and others promote terminal Teff cell differentiation by operating in the context of an “effector” or early activation epigenetic landscape. TCF-1 functions to antagonize this terminal Teff cell differentiation, perhaps in part through restraining the cell cycle and/or promoting expression of TF-like Eomes to blunt the activity of T-bet. PD-1 could complement this activity by helping to preserve the TCF-1⁺ subset. This early role of TCF-1 and PD-1 could then allow sufficient time for the Tox-dependent epigenetic remodeling toward mature Tex cells to occur over the first 1–2 weeks of chronic antigen exposure. One could then consider that the previous role of TFs such as T-bet in established exhaustion (Doering et al., 2012; Kao et al., 2011; Paley et al., 2012) could manifest differently than the effector-phase role because at these later time points, these TF are operating in an exhaustion epigenetic landscape rather than an effector epigenetic landscape. Such a model would explain the temporally distinct roles of T-bet in promoting expression of genes such as *Havcr2* (encoding Tim-3) early in infection while repressing expression of Tim-3 in established exhaustion (Kao et al., 2011). Although the studies presented here help clarify these early fate decisions in establishing Tex cells, it will be important in the future to further investigate the developmental relationships and TF cascades in the later stages of exhaustion.

Together, these studies identify the early events in initially establishing the Tex branch of CD8 T cell differentiation during chronic infection. Key features of this model were also observed in tumor models. We identified an early role for TCF-1 and defined the transcriptional circuitry linked to TCF-1 at this time point. These data extend our understanding of the role of TCF-1 in established exhaustion to the initial formation of Tex precursor cells. Moreover, our data indicate that Teff and Tex are dichotomous branches of CD8 T cell differentiation in settings of chronic antigen stimulation. The data presented here are consistent with studies demonstrating that Tex cells in humans are the major population in TILs, are the major cell type responding to PD-1 blockade, and are distinct from Teff even after PD-1-blockade-mediated reinvigoration (Bengsch et al., 2018; Guo et al., 2018; Huang et al., 2019; 2017; Zhang et al., 2018; Zheng et al., 2017). Thus, these findings highlight the distinction between Teff and Tex cells, define underlying molecular mechanisms for this distinction, and could have implications for which types of T cells are optimal targets for immunotherapy for cancer and other chronic diseases.

STAR★METHODS

Detailed methods are provided in the online version of this paper and include the following:

- KEY RESOURCES TABLE
- LEAD CONTACT AND MATERIALS AVAILABILITY
- METHOD DETAILS
 - Mice
 - Virus infection and tumor challenge experiments
 - Cell culture and *in vitro* stimulation
 - Retroviral vector (RV) experiments
 - Flow cytometry and sorting
 - Single cell RNA sequencing
 - RNA isolation and qPCR
 - Western blot
 - Immunofluorescence
 - Computational analysis of single cell RNA sequencing data
- STATISTICAL ANALYSIS

SUPPLEMENTAL INFORMATION

Supplemental Information can be found online at <https://doi.org/10.1016/j.immuni.2019.09.013>.

ACKNOWLEDGMENTS

We thank the Wherry lab for helpful discussions. This work was supported by NIH grants (AI105343, AI117950, AI082630, AI112521, AI115712, AI108545, and CA210944) and Stand Up 2 Cancer funding to E.J.W.; NIH grant HG009518 to H.J.; NIH grant CA234842 to Z. Chen; NIH grant AI114852 to R.S.H.; and NIH grant CA009140 to J.R.G. E.J.W. is supported by the Parker Institute for Cancer Immunotherapy, which supports the cancer immunology program at UPenn; S.F.N. is supported by an Australia NH&MRC C.J. Martin Fellowship (1111469) and the Mark Foundation Momentum Fellowship; and J.R.G. is supported by Cancer Research Institute-Mark Foundation Fellowship.

AUTHOR CONTRIBUTIONS

Z. Chen and E.J.W. designed the complete study; Z. Chen performed the experiments with the help of S.F.N., Z. Cai, A.E.B., J.E.W., J.-C.B., J.R.G., E.S., and C.W.L.; Z. Chen and Z.J. performed scRNA-seq and computational analysis with R.S., S.M., R.S.H., and L.V.; Z. Chen and Z.J. designed the STIP analysis method with the support of H.J.; S.M. and Z. Chen performed STIP analysis with motif analysis with help from O.K.; Z. Chen, J.J., M.K., and L.M. performed RV generation with the support of G.V.; B.B. provided the exhaustion-specific gene-list analysis; S.X. performed western blot with the support of X.Y.; C.X. performed immunofluorescence with the support of S.B.; J.E.W. and O.K. provided support for *in vitro* culture conditions; A.-C.H., J.E.W., and S.F.N. made key editorial contributions to the manuscript; and Z. Chen, Z.J., and E.J.W. wrote the manuscript.

DECLARATION OF INTERESTS

E.J.W. has consulting agreements with and/or is on the scientific advisory board for Merck, Roche, Pieris, Elstar, and Surface Oncology. E.J.W. is a founder of Surface Oncology and Arsenal Biosciences. E.J.W. has a patent licensing agreement on the PD-1 pathway with Roche/Genentech.

Received: January 30, 2019

Revised: July 11, 2019

Accepted: September 16, 2019

Published: October 9, 2019

REFERENCES

- Adams, W.C., Chen, Y.-H., Kratchmarov, R., Yen, B., Nish, S.A., Lin, W.W., Rothman, N.J., Luchsinger, L.L., Klein, U., Busslinger, M., et al. (2016). Anabolism-Associated Mitochondrial Stasis Driving Lymphocyte Differentiation over Self-Renewal. *Cell Rep.* *17*, 3142–3152.
- Alfei, F., Kanev, K., Hofmann, M., Wu, M., Ghoneim, H.E., Roelli, P., Utschneider, D.T., von Hoesslin, M., Cullen, J.G., Fan, Y., Eisenberg, V., et al. (2019). TOX reinforces the phenotype and longevity of exhausted T cells in chronic viral infection. *Nature* *571*, 265–269.
- Anastas, J.N., and Moon, R.T. (2013). WNT signalling pathways as therapeutic targets in cancer. *Nat Rev Cancer* *13*, 11–26.
- Angelosanto, J.M., Blackburn, S.D., Crawford, A., and Wherry, E.J. (2012). Progressive loss of memory T cell potential and commitment to exhaustion during chronic viral infection. *J. Virol.* *86*, 8161–8170.
- Barber, D.L., Wherry, E.J., Masopust, D., Zhu, B., Allison, J.P., Sharpe, A.H., Freeman, G.J., and Ahmed, R. (2006). Restoring function in exhausted CD8 T cells during chronic viral infection. *Nature* *439*, 682–687.
- Bensch, B., Ohtani, T., Khan, O., Setty, M., Manne, S., O'Brien, S., Gherardini, P.F., Herati, R.S., Huang, A.C., Chang, K.-M., et al. (2018). Epigenomic-Guided Mass Cytometry Profiling Reveals Disease-Specific Features of Exhausted CD8 T Cells. *Immunity* *48*, 1029–1045.e5.
- Blackburn, S.D., Shin, H., Freeman, G.J., and Wherry, E.J. (2008). Selective expansion of a subset of exhausted CD8 T cells by alphaPD-L1 blockade. *Proc. Natl. Acad. Sci. USA* *105*, 15016–15021.
- Chen, Z., Stelekati, E., Kurachi, M., Yu, S., Cai, Z., Manne, S., Khan, O., Yang, X., and Wherry, E.J. (2017). miR-150 Regulates Memory CD8 T Cell Differentiation via c-Myb. *Cell Rep.* *20*, 2584–2597.
- Chen, J., López-Moyado, I.F., Seo, H., Lio, C.-W.J., Hempleman, L.J., Sekiya, T., Yoshimura, A., Scott-Browne, J.P., and Rao, A. (2019). NR4A transcription factors limit CAR T cell function in solid tumours. *Nature* *567*, 530–534.
- Crawford, A., Angelosanto, J.M., Kao, C., Doering, T.A., Odorizzi, P.M., Barnett, B.E., and Wherry, E.J. (2014). Molecular and transcriptional basis of CD4⁺ T cell dysfunction during chronic infection. *Immunity* *40*, 289–302.
- Doering, T.A., Crawford, A., Angelosanto, J.M., Paley, M.A., Ziegler, C.G., and Wherry, E.J. (2012). Network analysis reveals centrally connected genes and pathways involved in CD8⁺ T cell exhaustion versus memory. *Immunity* *37*, 1130–1144.
- Dominguez, C.X., Amezquita, R.A., Guan, T., Marshall, H.D., Joshi, N.S., Kleinstein, S.H., and Kaech, S.M. (2015). The transcription factors ZEB2 and T-bet cooperate to program cytotoxic T cell terminal differentiation in response to LCMV viral infection. *J. Exp. Med.* *212*, 2041–2056.
- Finak, G., McDavid, A., Yajima, M., Deng, J., Gersuk, V., Shalek, A.K., Slichter, C.K., Miller, H.W., McElrath, M.J., Prlic, M., et al. (2015). MAST: a flexible statistical framework for assessing transcriptional changes and characterizing heterogeneity in single-cell RNA sequencing data. *Genome Biol.* *16*, 278.
- Guan, T., Dominguez, C.X., Amezquita, R.A., Laidlaw, B.J., Cheng, J., Henaomejia, J., Williams, A., Flavell, R.A., Lu, J., and Kaech, S.M. (2018). ZEB1, ZEB2, and the miR-200 family form a counterregulatory network to regulate CD8⁺ T cell fates. *J. Exp. Med.* *215*, 1153–1168.
- Guo, X., Zhang, Y., Zheng, L., Zheng, C., Song, J., Zhang, Q., Kang, B., Liu, Z., Jin, L., Xing, R., et al. (2018). Global characterization of T cells in non-small-cell lung cancer by single-cell sequencing. *Nat. Med.* *24*, 978–985.
- Gupta, P.K., Godec, J., Wolski, D., Adland, E., Yates, K., Pauken, K.E., Cosgrove, C., Ledderose, C., Junger, W.G., Robson, S.C., et al. (2015). CD39 Expression Identifies Terminally Exhausted CD8⁺ T Cells. *PLoS Pathog.* *11*, e1005177.
- He, R., Hou, S., Liu, C., Zhang, A., Bai, Q., Han, M., Yang, Y., Wei, G., Shen, T., Yang, X., Xu, L., et al. (2016). Follicular CXCR5-expressing CD8(+) T cells curtail chronic viral infection. *Nature* *537*, 412–428.
- Herndler-Brandstetter, D., Ishigame, H., Shinnakasu, R., Plajer, V., Stecher, C., Zhao, J., Lietzenmayer, M., Kroehling, L., Takumi, A., Kometani, K., et al. (2018). KLRG1⁺ Effector CD8⁺ T Cells Lose KLRG1, Differentiate into All Memory T Cell Lineages, and Convey Enhanced Protective Immunity. *Immunity* *48*, 716–729.e8.
- Huang, A.C., Postow, M.A., Orlowski, R.J., Mick, R., Bengsch, B., Manne, S., Xu, W., Harmon, S., Giles, J.R., Wenz, B., Adamow, M., et al. (2017). T-cell invigoration to tumour burden ratio associated with anti-PD-1 response. *Nature* *545*, 60–65.
- Huang, A.C., Orlowski, R.J., Xu, X., Mick, R., George, S.M., Yan, P.K., Manne, S., Kraya, A.A., Wubbenhorst, B., Dorfman, L., et al. (2019). A single dose of neoadjuvant PD-1 blockade predicts clinical outcomes in resectable melanoma. *Nat. Med.* *25*, 454–461.
- Ichii, H., Sakamoto, A., Hatano, M., Okada, S., Toyama, H., Taki, S., Arima, M., Kuroda, Y., and Tokuhisa, T. (2002). Role for Bcl-6 in the generation and maintenance of memory CD8⁺ T cells. *Nat Immunol* *3*, 558–563.
- Im, S.J., Hashimoto, M., Gerner, M.Y., Lee, J., Kissick, H.T., Burger, M.C., Shan, Q., Hale, J.S., Lee, J., Nasti, T.H., Sharpe, A.H., et al. (2016). Defining CD8⁺ T cells that provide the proliferative burst after PD-1 therapy. *Nature* *537*, 417–421.
- Intlekofer, A.M., Takemoto, N., Wherry, E.J., Longworth, S.A., Northrup, J.T., Palanivel, V.R., Mullen, A.C., Gasink, C.R., Kaech, S.M., Miller, J.D., Gapin, L., et al. (2005). Effector and memory CD8⁺ T cell fate coupled by T-bet and eomesodermin. *Nat Immunol* *6*, 1236–1244.
- Intlekofer, A.M., Banerjee, A., Takemoto, N., Gordon, S.M., Dejong, C.S., Shin, H., Hunter, C.A., Wherry, E.J., Lindsten, T., and Reiner, S.L. (2008). Anomalous type 17 response to viral infection by CD8⁺ T cells lacking T-bet and eomesodermin. *Science* *321*, 408–411.
- Ioannidis, V., Beermann, F., Clevers, H., and Held, W. (2001). The β -catenin-TCF-1 pathway ensures CD4⁺CD8⁺ thymocyte survival. *Nat Immunol* *2*, 691–697.
- Jeannot, G., Boudousquie, C., Gardiol, N., Kang, J., Huelsken, J., and Held, W. (2010). Essential role of the Wnt pathway effector Tcf-1 for the establishment of functional CD8 T cell memory. *Proc. Natl. Acad. Sci. USA* *107*, 9777–9782.
- Ji, Z., and Ji, H. (2016). TSCAN: Pseudo-time reconstruction and evaluation in single-cell RNA-seq analysis. *Nucleic Acids Res.* *44*, e117.
- Joshi, N.S., Cui, W., Chandele, A., Lee, H.K., Urso, D.R., Hagman, J., Gapin, L., and Kaech, S.M. (2007). Inflammation directs memory precursor and short-lived effector CD8(+) T cell fates via the graded expression of T-bet transcription factor. *Immunity* *27*, 281–295.
- Kaech, S.M., and Cui, W. (2012). Transcriptional control of effector and memory CD8⁺ T cell differentiation. *Nat Rev Immunol* *12*, 749–761.
- Kaech, S.M., Tan, J.T., Wherry, E.J., Konieczny, B.T., Surh, C.D., and Ahmed, R. (2003). Selective expression of the interleukin 7 receptor identifies effector CD8 T cells that give rise to long-lived memory cells. *Nat Immunol* *4*, 1191–1198.
- Kallies, A., Xin, A., Belz, G.T., and Nutt, S.L. (2009). Blimp-1 transcription factor is required for the differentiation of effector CD8(+) T cells and memory responses. *Immunity* *31*, 283–295.
- Kamphorst, A.O., Wieland, A., Nasti, T., Yang, S., Zhang, R., Barber, D.L., Konieczny, B.T., Daugherty, C.Z., Koenig, L., Yu, K., et al. (2017). Rescue of exhausted CD8 T cells by PD-1-targeted therapies is CD28-dependent. *Science* *355*, 1423–1427.
- Kao, C., Oestreich, K.J., Paley, M.A., Crawford, A., Angelosanto, J.M., Ali, M.-A.A., Intlekofer, A.M., Boss, J.M., Reiner, S.L., Weinmann, A.S., and Wherry, E.J. (2011). Transcription factor T-bet represses expression of the inhibitory receptor PD-1 and sustains virus-specific CD8⁺ T cell responses during chronic infection. *Nat Immunol* *12*, 663–671.
- Khan, O., Giles, J.R., McDonald, S., Manne, S., Ngiew, S.F., Patel, K.P., Werner, M.T., Huang, A.C., Alexander, K.A., Wu, J.E., Attanasio, J., et al. (2019). TOX transcriptionally and epigenetically programs CD8⁺ T cell exhaustion. *Nature* *571*, 211–218.
- Knight, D.A., Ngiew, S.F., Li, M., Parmenter, T., Mok, S., Cass, A., Haynes, N.M., Kinross, K., Yagita, H., Koya, R.C., et al. (2016). Host immunity contributes to the anti-melanoma activity of BRAF inhibitors. *J. Clin. Invest.* *126*, 402–403.
- Kurachi, M., Barnitz, R.A., Yosef, N., Odorizzi, P.M., Dilorio, M.A., Lemieux, M.E., Yates, K., Godec, J., Klatt, M.G., Regev, A., Wherry, E.J., et al. (2014). The transcription factor BATF operates as an essential differentiation checkpoint in early effector CD8⁺ T cells. *Nat Immunol* *15*, 373–383.

- Kurachi, M., Kurachi, J., Chen, Z., Johnson, J., Khan, O., Bengsch, B., Stelekati, E., Attanasio, J., McLane, L.M., Tomura, M., Ueha, S., et al. (2017). Optimized retroviral transduction of mouse T cells for in vivo assessment of gene function. *Nat Protoc* 12, 1980–1998.
- Lin, W.-H.W., Adams, W.C., Nish, S.A., Chen, Y.-H., Yen, B., Rothman, N.J., Kratchmarov, R., Okada, T., Klein, U., and Reiner, S.L. (2015). Asymmetric PI3K Signaling Driving Developmental and Regenerative Cell Fate Bifurcation. *Cell Rep.* 13, 2203–2218.
- Lin, W.W., Nish, S.A., Yen, B., Chen, Y.-H., Adams, W.C., Kratchmarov, R., Rothman, N.J., Bhandoola, A., Xue, H.-H., and Reiner, S.L. (2016). CD8⁺ T Lymphocyte Self-Renewal during Effector Cell Determination. *Cell Rep.* 17, 1773–1782.
- Liu, X., Wang, Y., Lu, H., Li, J., Yan, X., Xiao, M., Hao, J., Alekseev, A., Khong, H., Chen, T., Huang, R., et al. (2019). Genome-wide analysis identifies NR4A1 as a key mediator of T cell dysfunction. *Nature* 567, 525–529.
- Lun, A.T.L., Bach, K., and Marioni, J.C. (2016). Pooling across cells to normalize single-cell RNA sequencing data with many zero counts. *Genome Biol.* 17, 75.
- Man, K., Gabriel, S.S., Liao, Y., Gloury, R., Preston, S., Henstridge, D.C., Pellegrini, M., Zehn, D., Berberich-Siebel, F., Febbraio, M.A., et al. (2017). Transcription Factor IRF4 Promotes CD8⁺ T Cell Exhaustion and Limits the Development of Memory-like T Cells during Chronic Infection. *Immunity* 47, 1129–1141.e5.
- Martinez, G.J., Pereira, R.M., Äijö, T., Kim, E.Y., Marangoni, F., Pipkin, M.E., Togher, S., Heissmeyer, V., Zhang, Y.C., Crotty, S., et al. (2015). The transcription factor NFAT promotes exhaustion of activated CD8⁺ T cells. *Immunity* 42, 265–278.
- McLean, C.Y., Bristol, D., Hiller, M., Clarke, S.L., Schaar, B.T., Lowe, C.B., Wenger, A.M., and Bejerano, G. (2010). GREAT improves functional interpretation of cis-regulatory regions. *Nat Biotechnol.* 28, 495–501.
- Mognol, G.P., Spreafico, R., Wong, V., Scott-Browne, J.P., Togher, S., Hoffmann, A., Hogan, P.G., Rao, A., and Trifari, S. (2017). Exhaustion-associated regulatory regions in CD8⁺ tumor-infiltrating T cells. *Proc. Natl. Acad. Sci. USA* 114, E2776–E2785.
- Odorizzi, P.M., Pauken, K.E., Paley, M.A., Sharpe, A., and Wherry, E.J. (2015). Genetic absence of PD-1 promotes accumulation of terminally differentiated exhausted CD8⁺ T cells. *J. Exp. Med.* 212, 1125–1137.
- Omlusik, K.D., Nadjisombati, M.S., Shaw, L.A., Yu, B., Milner, J.J., and Goldrath, A.W. (2018). Sustained Id2 regulation of E proteins is required for terminal differentiation of effector CD8⁺ T cells. *J. Exp. Med.* 215, 773–783.
- Paley, M.A., Kroy, D.C., Odorizzi, P.M., Johnnidis, J.B., Dolfi, D.V., Barnett, B.E., Bikoff, E.K., Robertson, E.J., Lauer, G.M., Reiner, S.L., and Wherry, E.J. (2012). Progenitor and terminal subsets of CD8⁺ T cells cooperate to contain chronic viral infection. *Science* 338, 1220–1225.
- Paley, M.A., Gordon, S.M., Bikoff, E.K., Robertson, E.J., Wherry, E.J., and Reiner, S.L. (2013). Technical Advance: Fluorescent reporter reveals insights into eomesodermin biology in cytotoxic lymphocytes. *J. Leukoc. Biol.* 93, 307–315.
- Pauken, K.E., Sammons, M.A., Odorizzi, P.M., Manne, S., Godec, J., Khan, O., Drake, A.M., Chen, Z., Sen, D.R., Kurachi, M., et al. (2016). Epigenetic stability of exhausted T cells limits durability of reinvigoration by PD-1 blockade. *Science* 354, 1160–1165.
- Philip, M., Fairchild, L., Sun, L., Horste, E.L., Camara, S., Shakiba, M., Scott, A.C., Viale, A., Lauer, P., Merghoub, T., Hellmann, M.D., et al. (2017). Chromatin states define tumour-specific T cell dysfunction and reprogramming. *Nature* 545, 452–456.
- Qiu, X., Hill, A., Packer, J., Lin, D., Ma, Y.-A., and Trapnell, C. (2017). Single-cell mRNA quantification and differential analysis with Census. *Nat Methods* 14, 309–315.
- Quigley, M., Pereyra, F., Nilsson, B., Porichis, F., Fonseca, C., Eichbaum, Q., Julg, B., Jesneck, J.L., Brosnahan, K., Imam, S., et al. (2010). Transcriptional analysis of HIV-specific CD8⁺ T cells shows that PD-1 inhibits T cell function by upregulating BATF. *Nat. Med.* 16, 1147–1151.
- Rutishauser, R.L., Martins, G.A., Kalachikov, S., Chandele, A., Parish, I.A., Meffre, E., Jacob, J., Calame, K., and Kaech, S.M. (2009). Transcriptional repressor Blimp-1 promotes CD8(+) T cell terminal differentiation and represses the acquisition of central memory T cell properties. *Immunity* 31, 296–308.
- Sade-Feldman, M., Yizhak, K., Bjorgaard, S.L., Ray, J.P., de Boer, C.G., Jenkins, R.W., Lieb, D.J., Chen, J.H., Frederick, D.T., Barzily-Rokni, M., et al. (2018). Defining T Cell States Associated with Response to Checkpoint Immunotherapy in Melanoma. *Cell* 175, 998–1013.e20.
- Schietinger, A., Philip, M., Krisnawan, V.E., Chiu, E.Y., Delrow, J.J., Basom, R.S., Lauer, P., Brockstedt, D.G., Knoblaugh, S.E., Hämmerling, G.J., et al. (2016). Tumor-Specific T Cell Dysfunction Is a Dynamic Antigen-Driven Differentiation Program Initiated Early during Tumorigenesis. *Immunity* 45, 389–401.
- Scott, A.C., Dündar, F., Zumbo, P., Chandran, S.S., Klebanoff, C.A., Shakiba, M., Trivedi, P., Menocal, L., Appleby, H., Camara, S., et al. (2019). TOX is a critical regulator of tumour-specific T cell differentiation. *Nature* 571, 270–274.
- Sen, D.R., Kaminski, J., Barnitz, R.A., Kurachi, M., Gerdemann, U., Yates, K.B., Tsao, H.-W., Godec, J., LaFleur, M.W., Brown, F.D., et al. (2016). The epigenetic landscape of T cell exhaustion. *Science* 354, 1165–1169.
- Seo, H., Chen, J., González-Avalos, E., Samaniego-Castruita, D., Das, A., Wang, Y.H., López-Moyado, I.F., Georges, R.O., Zhang, W., Onodera, A., et al. (2019). TOX and TOX2 transcription factors cooperate with NR4A transcription factors to impose CD8⁺ T cell exhaustion. *Proc. Natl. Acad. Sci. USA* 116, 12410–12415.
- Stelekati, E., Chen, Z., Manne, S., Kurachi, M., Ali, M.-A., Lewy, K., Cai, Z., Nzingha, K., McLane, L.M., Hope, J.L., et al. (2018). Long-Term Persistence of Exhausted CD8 T Cells in Chronic Infection Is Regulated by MicroRNA-155. *Cell Rep.* 23, 2142–2156.
- Utzschneider, D.T., Charmoy, M., Chennupati, V., Pousse, L., Ferreira, D.P., Calderon-Copete, S., Danilo, M., Alfei, F., Hofmann, M., Wieland, D., et al. (2016). T Cell Factor 1-Expressing Memory-like CD8(+) T Cells Sustain the Immune Response to Chronic Viral Infections. *Immunity* 45, 415–427.
- Weber, B.N., Chi, A.W.-S., Chavez, A., Yashiro-Ohtani, Y., Yang, Q., Shestova, O., and Bhandoola, A. (2011). A critical role for TCF-1 in T-lineage specification and differentiation. *Nature* 476, 63–68.
- Wherry, E.J., Teichgräber, V., Becker, T.C., Masopust, D., Kaech, S.M., Antia, R., von Andrian, U.H., and Ahmed, R. (2003). Lineage relationship and protective immunity of memory CD8 T cell subsets. *Nat Immunol* 4, 225–234.
- Wherry, E.J., Ha, S.-J., Kaech, S.M., Haining, W.N., Sarkar, S., Kalia, V., Subramaniam, S., Blattman, J.N., Barber, D.L., and Ahmed, R. (2007). Molecular signature of CD8⁺ T cell exhaustion during chronic viral infection. *Immunity* 27, 670–684.
- Wu, T., Ji, Y., Moseman, E.A., Xu, H.C., Mangani, M., Kirby, M., Anderson, S.M., Handon, R., Kenyon, E., Elkahloun, A., Wu, W., et al. (2016). The TCF1-Bcl6 axis counteracts type I interferon to repress exhaustion and maintain T cell stemness. *Sci Immunol* 1, eaai8593.
- Yang, C.Y., Best, J.A., Knell, J., Yang, E., Sheridan, A.D., Jesionek, A.K., Li, H.S., Rivera, R.R., Lind, K.C., D’Cruz, L.M., Watowich, S.S., et al. (2011). The transcriptional regulators Id2 and Id3 control the formation of distinct memory CD8⁺ T cell subsets. *Nat Immunol* 12, 1221–1229.
- Yao, C., Sun, H.-W., Lacey, N.E., Ji, Y., Moseman, E.A., Shih, H.-Y., Heuston, E.F., Kirby, M., Anderson, S., Cheng, J., Khan, O., et al. (2019). Single-cell RNA-seq reveals TOX as a key regulator of CD8⁺ T cell persistence in chronic infection. *Nat Immunol* 20, 890–901.
- Yee, T.W. (2015). Vector Generalized Linear and Additive Models: With an Implementation in R. (Springer).
- Zhang, L., Yu, X., Zheng, L., Zhang, Y., Li, Y., Fang, Q., Gao, R., Kang, B., Zhang, Q., Huang, J.Y., Konno, H., et al. (2018). Lineage tracking reveals dynamic relationships of T cells in colorectal cancer. *Nature* 564, 268–272.
- Zheng, C., Zheng, L., Yoo, J.-K., Guo, H., Zhang, Y., Guo, X., Kang, B., Hu, R., Huang, J.Y., Zhang, Q., et al. (2017). Landscape of Infiltrating T Cells in Liver Cancer Revealed by Single-Cell Sequencing. *Cell* 169, 1342–1356.e16.
- Zhou, X., Yu, S., Zhao, D.-M., Harty, J.T., Badovinac, V.P., and Xue, H.-H. (2010). Differentiation and persistence of memory CD8(+) T cells depend on T cell factor 1. *Immunity* 33, 229–240.

STAR★METHODS

KEY RESOURCES TABLE

REAGENT or RESOURCE	SOURCE	IDENTIFIER
Mouse strains		
C57BL/6	Charles River	N/A
CD45.1 ⁺ C57BL/6	Charles River	N/A
BALB/C	Charles River	N/A
TCR $\alpha^{-/-}$; P14 TCRV α 2V β 8	The Jackson Lab	Stock No. 37394-JAX
<i>Pdcd1</i> ^{-/-}	Odorizzi et al., 2015	N/A
<i>Eomes</i> ^{GFP}	Paley et al., 2013	N/A
<i>Tcf7</i> ^{flox/flox}	Weber et al., 2011	N/A
<i>Eomes</i> ^{flox/flox}	Intlekofer et al., 2008	N/A
<i>Cd4</i> ^{CRE}	The Jackson Lab	Stock No. 022071
<i>Rosa26</i> -CRE ^{ERT2}	The Jackson Lab	Stock No: 008463
Flow cytometry reagents		
Live/Dead Aqua Dye	Thermofisher	Cat#L34957
Live/Dead Zombie NIR Dye	BioLegend	Cat#423106
Anti-Mouse KLRG1(2F1)	BD Biosciences	Cat# 561619, RRID: AB_10898017
Anti-Mouse CD127(A7R34)	BioLegend	Cat# 135016, RRID: AB_1937261
Anti-Mouse CD8(53-6.7)	BioLegend	Cat# 100742, RRID: AB_2563056
Anti-Mouse CD44(IM7)	BioLegend	Cat# 103059, RRID: AB_2571953
Anti-Mouse CD45.1(A20)	BioLegend	Cat# 110724, RRID: AB_493733; Cat# 110716, RRID: AB_313505
Anti-Mouse CD45.2(104)	BioLegend	Cat# 109828, RRID: AB_893350; Cat# 109823, RRID: AB_830788
Anti-Mouse CD122(TM-b1)	Thermofisher	Cat# 48-1222-80, RRID: AB_2016628
Anti-Mouse Ly108(330-AJ)	BioLegend	Cat# 134608, RRID: AB_2188093; Cat# 134605, RRID: AB_1659258
Anti-Mouse Tim-3(RMT3-23)	BioLegend	Cat# 119721, RRID: AB_2616907
Anti-Mouse CD39(24DMS1)	Thermofisher	Cat# 46-0391-80, RRID: AB_10717513
Anti-Mouse PD-1(RMP1-30)	BioLegend	Cat# 109109, RRID: AB_572016
Anti-Mouse TCF-1(S33-966)	BD Biosciences	Cat# 564217, RRID: AB_2687845
Anti-Mouse TCF-1(C63D9)	Cell Signaling Technology	Cat# 14456, RRID: AB_2199302
Anti-Mouse T-bet(4B10)	BioLegend	Cat# 644808, RRID: AB_1595479
Anti-Mouse <i>Eomes</i> (Dan11mag)	Thermofisher	Cat# 50-4875-80, RRID: AB_2574226
Anti-Mouse Ki67(16A8)	BioLegend	Cat# 652420, RRID: AB_2564285
Anti-Mouse Bcl-2(A19-3)	BD Biosciences	Cat# 556537, RRID: AB_396457
Anti-Mouse Bim(C34C5)	Cell Signaling Technology	Cat# 2933, RRID: AB_1030947
Anti-Mouse CD107a(1D4B)	BioLegend	Cat# 121606, RRID: AB_572007
Anti-Mouse TNF α (MP6-XT22)	BioLegend	Cat# 506328, RRID: AB_2562902
Anti-Mouse IFN γ (XMG1.2)	BD Biosciences	Cat# 560661, RRID: AB_1727534
Anti-Mouse Gzmb(GB11)	Thermofisher	Cat# GRB17, RRID: AB_2536540
LCMV D ^b GP33 tetramer	NIH	Conjugated in house
LCMV D ^b GP276 tetramer	NIH	Conjugated in house
BD GolgiStop	Thermofisher	Cat# 554724
BD GolgiPlug	Thermofisher	Cat#555029
Foxp3 Transcription Factor Staining Buffer Kit	Thermofisher	Cat# A25866A

(Continued on next page)

Continued

REAGENT or RESOURCE	SOURCE	IDENTIFIER
Experimental Models: LCMV		
LCMV Clone13 (Cl13)	Rafi Ahmed	Grew up in house
LCMV Armstrong (Arm)	Rafi Ahmed	Grew up in house
Experimental Models: Tumor Cell Lines		
CT26	ATCC	Cat# CRL-2638, RRID: CVCL_7256
Mouse treatment reagents		
Anti-mouse CD4 Mab (GK1.5)	Bioxcell	Cat# BE0003-1
Tamoxifen	Sigma-aldrich	Cat# T5648-1G
<i>In vitro</i> culture and retroviral transduction reagents		
Recombinant human IL-2	NIH	N/A
Anti-Mouse CD3(145-2C11)	BioLegend	Cat# 100302, RRID: AB_312667
Anti-Mouse CD28(37.51)	ThermoFisher	Cat# 16-0281-82, RRID: AB_468921
LCMV peptide GP ₃₃₋₄₁	NIH	N/A
EasySep™ Mouse CD8+ T Cell Isolation Kit	STEMCELL Technologies	Cat# 19853
RPMI-1640 medium	Corning/Mediatech	Cat# 10-040-CV
HI Fetal Bovine Serum	ThermoFisher	Cat# 26170-043
HEPES	ThermoFisher	Cat# 15630080
Non-Essential Amino Acids	ThermoFisher	Cat# 11140050
Penicillin-Streptomycin	ThermoFisher	Cat# 15140122
β-mercaptoethanol	Sigma-Aldrich	Cat# M6250-500ML
Opti-MEM	ThermoFisher	Cat# 31985088
Polybrene	Sigma-Aldrich	Cat# TR-1003-G
Lipofectamine™ 3000 Transfection Reagent	ThermoFisher	Cat# L3000001
cDNA constructs		
TCF-1 p33 cDNA	OriGene	MR226713
TCF-1 p33 overexpression vector	In this paper	N/A
TCF-1 p45 overexpression vector	In this paper	N/A
c-Myb overexpression vector	Chen et al. 2017	N/A
T-bet overexpression vector	In this paper	N/A
Empty-VEX retroviral vector	Kurachi et al. 2017	N/A
Single cell RNA Sequencing		
Chromium Single Cell 3' Library & Gel Bead Kit v2	10X Genomics	Cat# PN-120267
Chromium Single Cell A Chip Kit	10X Genomics	Cat# PN-1000009
Chromium i7 Multiplex Kit	10X Genomics	Cat# PN-120262
Dynabeads™ MyOne™ Silane	ThermoFisher	Cat# 37002D
SPRIselect Reagent Kit	Beckman Coulter	Cat#B23318
10% Tween 20	Bio-Rad	Cat#1610781
Glycerin (glycerol), 50% (v/v) Aqueous Solution	Ricca Chemical Company	Cat# 3290-32
KAPA NGS quantification kit	KAPABiosystems	Cat# KK4824
NextSeq 500/550 High Output Kit v2.5 (150 Cycles)	Illumina	Cat# 20024907
RT-QPCR		
iTaq™ Universal SYBR® Green Supermix	Bio-Rad	Cat# 1725121
Eomes Forward Primer GCGCATGTTTCCTTCTTGAG	In this paper	N/A
Eomes Reverse Primer GGTCGGCCAGAACCACTTC	In this paper	N/A
c-Myb Forward Primer AGACCCCGACACAGCATCTA	Chen et al., 2017	N/A

(Continued on next page)

Continued

REAGENT or RESOURCE	SOURCE	IDENTIFIER
c-Myb Reverse Primer CAGCAGCCCATCGTAGTCAT	Chen et al., 2017	N/A
GAPDH Forward Primer AGGTCGGTGTGAACGGATTTG	Chen et al., 2017	N/A
GAPDH Reverse Primer TGTAGACCATGTAGTTGAGGTCA	Chen et al., 2017	N/A
Western Blot		
Anti-c-Myb (C19)	Santa Cruz,	Cat# sc-517, RRID: AB_2148017
Anti-Actin	Sigma-Aldrich	Cat# A5316, RRID: AB_476743
Immunofluorescence		
Anti- γ H2AX	Abcam	Cat# ab2893, RRID: AB_303388
Anti- γ H2AX	Millipore	Cat# 05-636, RRID: AB_309864
Goat anti-Rabbit IgG (H+L) Highly Cross-Adsorbed Secondary Antibody, Alexa Fluor Plus 647	ThermoFisher	Cat# A32733, RRID: AB_2633282
Goat anti-Mouse IgG (H+L) Highly Cross-Adsorbed Secondary Antibody, Alexa Fluor Plus 647	ThermoFisher	Cat# A32728, RRID: AB_2633277
ProLong™ Gold Antifade Mountant	ThermoFisher	Cat# P10144
Computational analysis		
Cell Ranger	10X Genomics	https://support.10xgenomics.com/single-cell-gene-expression/software/pipelines/latest/installation
Scran	Lun et al., 2016	https://bioconductor.org/packages/release/bioc/html/scran.html
MAST	Finak et al., 2015	https://www.bioconductor.org/packages/release/bioc/html/MAST.html
VGAM	Yee, 2015	https://cran.r-project.org/web/packages/VGAM/index.html
Monocle-2	Qiu et al., 2017	http://cole-trapnell-lab.github.io/monocle-release/docs/
TSCAN	Ji and Ji, 2016	https://www.bioconductor.org/packages/release/bioc/html/TSCAN.html
STIP	In this paper	https://github.com/zji90/STIP
The GREAT software	McLean et al., 2010	http://great.stanford.edu/public/html
Cytoscape(3.7.1)	Cytoscape	https://cytoscape.org
DAVID GO analysis (6.8)	LHRI	https://david.ncifcrf.gov/tools.jsp
Statistical Analysis		
Prism 7	GraphPad Software	N/A
Datasets		
D8 p.i. single cell RNA Sequencing on P14 cells	In this paper	https://www.ncbi.nlm.nih.gov/geo/query/acc.cgi?acc=GSE131535
D8 p.i. ATAC-Sequencing on P14 cells	Sen et al., 2016.	https://www.ncbi.nlm.nih.gov/geo/query/acc.cgi?acc=GSE87646
Mouse TF motifs	HOCOMOCO V11 mouse	http://hocomoco11.autosome.ru
<i>Klrg1</i> ⁺ DiffGene Index	Herndler-Brandstetter et al., 2018	https://www.ncbi.nlm.nih.gov/geo/query/acc.cgi?acc=GSE110707
<i>Havcr2</i> ⁺ <i>Entpd1</i> ⁺ DiffGene index and <i>Tcf7</i> ⁺ <i>Pdcd1</i> ⁺ DiffGene index	Sade-Feldman et al., 2018	https://www.ncbi.nlm.nih.gov/geo/query/acc.cgi?acc=GSE120575

LEAD CONTACT AND MATERIALS AVAILABILITY

Further information and requests for resources should be directed to and will be fulfilled by the Lead Contact, E. John Wherry (wherry@penntermedicine.upenn.edu).

METHOD DETAILS

Mice

Pdcd1^{-/-} (Odorizzi et al., 2015), *Eomes*^{GFP} (Paley et al., 2013), *Tcf7*^{flox/flox} (Weber et al., 2011) and *Eomes*^{flox/flox} (Intlekofer et al., 2008) mice have been described. *Cd4*^{CRE} and Rosa26-CRE^{ERT2} mice were purchased from Jackson Laboratory. *Tcf7*^{flox/flox} mice were bred to *Cd4*^{CRE} mice and TCR transgenic P14 C57BL/6 mice (TCR specific for LCMV D^bGP₃₃₋₄₁). *Eomes*^{flox/flox} mice were bred to Rosa26-CRE^{ERT2} mice and TCR transgenic P14 C57BL/6 mice. *Pdcd1*^{-/-} and *Eomes*^{GFP} mice were bred to TCR transgenic P14 C57BL/6 mice. 6-8 week-old C57BL/6 Ly5.2CR (CD45.1) or C57BL/6 (CD45.2) mice were purchased from NCI. Both male and female mice were used. All mice were used in accordance with Institutional Animal Care and Use Committee guidelines for the University of Pennsylvania.

Virus infection and tumor challenge experiments

Mice were infected intraperitoneally (i.p.) with 2×10^5 plaque-forming units (PFU) LCMV Armstrong or intravenously (i.v.) with 4×10^6 PFU LCMV Cl13. The mice of Cl13ΔCD4 group received 200 μg GK1.5/mouse i.p. treatment on day -1 and day 1 post Cl13 infection. The mice of inducible genetic deletion group received 2mg tamoxifen/mouse i.p. everyday on day9 to day13 post Cl13 infection. For tumor studies, 2×10^5 CT26 cells were subcutaneously injected into BALB/C mice. Established CT26 tumors (D8 post transfer) were excised and processed for flow cytometry as described (Knight et al., 2016). In brief, tumors were digested with 1 mg/mL collagenase D and 0.02 mg/mL DNaseI at 37°C.

Cell culture and *in vitro* stimulation

CD8 T cells were purified from spleens by negative selection using EasySep Mouse CD8+ T Cell Isolation Kit (STEMCELL Technologies) according to manufacturer's instructions. Cells were stimulated with 100 U/mL recombinant human IL-2, 1 μg/mL anti-mouse CD3ε, and 5 μg/mL anti-mouse CD28 in RPMI-1640 medium with 10% fetal bovine serum (FBS), 10 mM HEPES, 100 μM non-essential amino acids (NEAA), 50 U/mL penicillin, 50 μg/mL streptomycin, and 50 μM β-mercaptoethanol.

Retroviral vector (RV) experiments

The TCF-1 p33 (MR226713) cDNA clone was obtained from OriGene and the TCF-1 p45 cDNA clone was extended from the TCF-1 p33 cDNA using PCR. TCF-1 p33 or TCF-1 p45 cDNA were cloned into the MSCV-IRES-VEX plasmid. The c-Myb RV was constructed as described (Chen et al., 2017). The T-bet RV was constructed as described (Kao et al., 2011). RVs were produced in 293T cells with MSCV and pCL-Eco plasmids using Lipofectamine 3000. RV transduction was performed as described (Kurachi et al., 2017). Briefly, CD8 T cells were purified from spleens of P14 mice using EasySepTM Mouse CD8+ T Cell Isolation Kit. After 18-24 h of *in vitro* stimulation, P14 cells were transduced with RV in the presence of polybrene (0.5 μg/mL) during spin infection (2,000 g for 60 min at 32°C) following incubation at 37°C for 6 h. RV-transduced P14 cells were adoptively transferred into recipient mice that were infected 24 h prior to transfer.

Flow cytometry and sorting

For mouse experiments, tissues were processed, single cell suspensions obtained, and cells were stained as described (Wherry et al., 2003). Mouse cells were stained with LIVE/DEAD cell stain (Invitrogen) and with antibodies targeting surface or intracellular proteins. Intracellular cytokine staining was performed after 5 h *ex vivo* stimulation with GP₃₃₋₄₁ peptide in the presence of GolgiPlug, GolgiStop and anti-CD107a. After stimulation, cells were stained with surface antibodies, followed by fixation with Fixation/Permeabilization Buffer and then stained with intracellular antibodies for TNF, IFN-γ and GrzmB using Permeabilization Wash Buffer according to manufacturer's instructions. Flow cytometry was performed with an LSRII. Cell sorting experiments were performed with a BD-Aria sorter, with 70 micron nozzle and a 4°C circulating cool-down system.

Single cell RNA sequencing

P14 cells from spleens of naive or infected mice were isolated using EasySepTM Mouse CD8+ T Cell Isolation Kit. Cells were double-sorted for the CD8 CD45.2⁺(P14⁺) population into 1.5 mL Lo-Bind Eppendorf tubes with complete RPMI (10% FBS). 2×10^4 P14s were collected and washed with PBS twice before loading to a Chromium single cell sorting system (10X Genomics). Library construction was performed following the protocol of Chromium Single Cell 3' Library system, with a standard loading targeting 5×10^3 cells recovered. The final pooled library with 4 samples (Naive, Arm, Cl13 and Cl13ΔCD4) was sequenced on a NextSeq 500 using 1 pair-end high throughput FlowCell.

RNA isolation and qPCR

Total RNA was isolated using RNeasy micro kit from QIAGEN. QRT-PCR was performed using iTaqTM Universal SybrGreen Supermix from BioRad on the ViiA 7 Real-Time PCR System according to manufacturer's instructions.

Western blot

Cells were lysed in RIPA buffer and processed as described (Chen et al., 2017). Blots were stained for c-Myb (1:200 for antibody staining for 1 h at room temperature) and actin (1:5000 for secondary staining for 1 h at room temperature). Western blots were quantified by ImageJ.

Immunofluorescence

Cells were fixed in 4% paraformaldehyde in PBS for 30min at room temperature. After two PBS washes, cells were permeabilized with 0.5% Triton X-100 in PBS for 10min, followed by two additional PBS washes. Cells were then blocked in 10% BSA in PBS for 1 h at room temperature, and were incubated with γ H2AX antibodies (Abcam, ab2893, 1:200 or Millipore, 05-636, 1:100) in 5% BSA in PBS supplemented with 0.1% Tween 20 (PBST) overnight at 4°C. The next day, cells were washed 4X 10min with PBST, and then incubated with Alexa Fluor 647-conjugated secondary antibody in 5% BSA/PBST for 1 h at room temperature, followed by 4X 10min washes with PBST. Cells were then stained with 1 μ g/mL DAPI for 5min and washed twice with PBS. The coverslip was mounted with ProLong Gold, and imaged with Leica TCS SP8 fluorescent confocal microscope (63X).

Computational analysis of single cell RNA sequencing data

Data processing

Raw sequencing files were aligned to the mouse mm10 genome using Cell Ranger software (10x Genomics). Mitochondrial genes were removed and cells that had positive read counts of at least 1000 genes were retained. Scran (Lun et al., 2016) was used to normalize the raw gene expression counts and normalized expression values were used throughout the analysis.

ScRNA-Seq analysis

MAST (Finak et al., 2015) was used to perform differential analysis comparing gene expression of two cell clusters. GAM (in R package VGAM (Yee, 2015)) was used to fit the gene expression along a pseudotime trajectory. A Tobit family (lower threshold = 0.1) was used to account for potential dropout events. To determine whether expression of a gene changed significantly along the pseudotime trajectory, a likelihood ratio test was performed comparing the full model with an intersect-only null model. FDRs were calculated for p values of the likelihood ratio tests. A gene with FDR < 0.05 was determined to have differential expression along the pseudotime axis. Packages for pseudotime analysis include Monocle-2 (Qiu et al., 2017), TSCAN (Ji and Ji, 2016) and STIP (<https://github.com/zji90/STIP>). Briefly STIP functions as follows: Given a pseudotime trajectory and gene expression profiles, STIP first extracts the TFs for which expression changes significantly along the pseudotime trajectory. Expression of each gene is then standardized to have a mean of zero and variance of one across all cells. For each gene STIP then calculates the pseudotime point at which the standardized expression is zero (zero point). Only genes that have 1 or 2 zero points are retained. Finally it reorders genes based on expression patterns (monotone increasing, single peak, monotone decreasing) and the occurrence of the zero point within each pattern. One can then compare the correlations between different genes with a selected anchor gene (*Tcf7* in this study).

ATAC-Seq and Network Analysis

Open chromatin regions for each sample (Naive and D8 Cl13 samples as described (Sen et al., 2016)) were determined by peak calling using macs2v2.1.1 “callpeak” function at a q value of 0.01. For each peak identified, TF binding sites were scanned using the FIMO algorithm in the 100 bp centered around the summit of the peak, the TF motifs were obtained for MOUSE transcription factors (core) from HOCOMOCO V11 mouse. TF binding sites in these enhancers were linked to corresponding promoters/genes that were defined in a manner similar to the GREAT software, where each gene is assigned a basal regulatory domain that is defined as the promoter region and extended in both directions to the nearest gene basal domain but no more than 1000kb each direction. Network analysis was visualized using Cytoscape software (3.7.1).

Gene Ontology Analysis

For each cluster, a GO analysis was conducted comparing the top 100 genes that were highly differentially expressed and all the other genes in the dataset. GO analysis was performed using DAVID with default parameters.

Gene index generation

The *Klrg1+DiffGene* index was generated using bulk RNA-seq data (Herndler-Brandstetter et al., 2018). The comparison was between *KLRG1⁺exKLRG1⁺* versus *KLRG1⁻exKLRG1⁻* groups. We selected the entire set of differentially expressed coding genes with the FDR < 0.05. The *Havcr2⁺Entpd1⁺ DiffGene* index was generated using scRNA-seq (Sade-Feldman et al., 2018). The comparison was between the *Havcr2⁺Entpd1⁺* and the *Havcr2⁻Entpd1⁻* groups. We selected the top 100 differentially expressed coding genes that were higher in the *Havcr2⁺Entpd1⁺* group with an FDR < 0.05. The *Tcf7⁺Pdcd1⁺ DiffGene* index was generated using scRNA-seq (Sade-Feldman et al., 2018). The comparison was between the *Tcf7⁺Pdcd1⁺* and the *Tcf7⁻Pdcd1⁻* groups. We selected the top 100 differentially expressed coding genes that were higher in the *Tcf7⁺Pdcd1⁺* group with an FDR < 0.05.

STATISTICAL ANALYSIS

Statistical significance was calculated with unpaired two-tailed Student's t test or one-way ANOVA with Tukey's multiple comparisons test by Prism 7 (GraphPad Software). P values are reported in the figure legends.